UNIVERSITÀ DEGLI STUDI DI PADOVA
DIPARTIMENTO DI INGEGNERIA INDUSTRIALE
CORSO DI LAUREA MAGISTRALE IN INGEGNERIA CHIMICA E DEI PROCESSI INDUSTRIALI

Tesi di Laurea Magistrale in
Ingegneria Chimica e dei Processi Industriali

First-principles modeling of Solid Oxide Fuel Cells accounting for electrodes geometry and microstructure

Relatore: Prof. Paolo Canu

Correlatore: Ing. Nicola Zanetti

Laureando: FRANCESCO GIORDANO

ANNO ACCADEMICO 2019 – 2020

Abstract

In this work a 2-D isothermal axial-symmetric model of an electrolyte supported Solid Oxide Fuel Cell (SOFC) has been developed. This study is part of a collaboration between the department of Chemical Engineering and the department of Chemical Sciences at the University of Padua. The work starts from the geometrical characterization and the description of the manufacturing technique of the cell. Then, its representation on COMSOL Multiphysics is described as well. Subsequently, the model is implemented trying to describe the complex phenomena that occur within a SOFC through a first principles-based approach. Particularly, as regards the porous electrodes, these have been modeled as continuous and isotropic pseudo phases, characterized by effective properties. These properties depend on the microstructural features of the porous electrodes and they have been estimated using dedicated models - since anode and cathode are very different microstructurally - based on Percolation Theory. Kinetic and microstructural unknown parameters have been obtained using the Optimization module available in COMSOL Multiphysics. Successively, the validation of the model takes place thorough the comparison between the Electrochemical Impedance Spectroscopy (EIS) and Polarization (PC) curves, obtained experimentally and numerically. The model can appropriately simulate the functioning of the studied SOFC. Once the model has been validated, a sensitivity analysis on several parameters was carried out. The results of this analysis highlighted possible corrections to be made to the cell design, in order to improve its performance. Particularly, the thickness of the cathode used has proven to be strongly undersized.

Ringraziamenti

Alla fine di questo faticoso percorso è giusto ringraziare tutti quelli che mi son stati vicini, fisicamente e non, durante questo periodo padovano della mia vita. Innanzitutto, un enorme grazie va alla mia famiglia. Il loro contributo è stato fondamentale. Madre e Padre, così li chiamo scherzosamente, sono stati la mia fonte motivazionale ed economica in questi anni. Di questo gliene sono grato, non tutti hanno queste fortune. Qui a Padova non è stato sempre tutto rose e fiori, fortunatamente ho condiviso la casa – ed il percorso di studi – con il caro amico/collega Zuzù e, successivamente, l'aggiunta di mio fratello ha portato altro casino in questa casa di scoppiati urlatori - ed anche alla scomparsa prematura dei miei adorati pacchi di biscotti. Nonostante tutto, questa esperienza è stata davvero bella e mi ha notevolmente cambiato. Un grazie speciale va anche alla mia ragazza, con la quale ho potuto condividere la tristezza della distanza e la gioia nel riabbracciarci ogni volta che si presentava l'occasione di poter viaggiare. Parte della famiglia anche la mia cucciola di Labrador – ormai ha una certa età ma per me rimarrà sempre quello – Sally. Sei arrivata in un periodo particolare della mia vita, portando gioia e serenità. Inconsciamente hai preso parte a questo mio cammino: ricordo piacevolmente quando, ancora a Palermo, ti costringevo ad ascoltarmi mentre ripetevo prima dei vari esami sostenuti. Un grazie anche ai pochi ma buoni amici che ho, mi avete tenuto compagnia ed è stato bello organizzarci per poterci incontrare nelle varie città nelle quali siamo ormai dispersi. Truco, sappi che spero di non perdere la scommessa sul primo stipendio: mi rovinerebbe. Infine, un grazie a tutti quelli che in maniera più o meno velata hanno fatto parte della mia vita durante questo tragitto: dai colleghi ai professori fino alla signora della copisteria. In particolare, ringrazio il professore Paolo Canu per l'opportunità offertami ed il mio tutor Nicola per la disponibilità e competenza dimostrata.

Index

Introduction

The purpose of this thesis is to develop a model capable of simulating a Solid Oxide Fuel Cell (SOFC) manufactured and characterized, via electrochemical impedance spectroscopy and polarization curve, by the Chemistry Department of the University of Padua. In order to model the cell, the commercial finite element method software COMSOL Multiphysics is used. It is a powerful tool that allows the mathematical modeling of various phenomena, including the electrochemical ones. Therefore, this thesis combines the knowledge of chemists in manufacturing new promising materials for SOFC applications with the mathematical-modeling approach typical of engineers.

This thesis is divided into four chapters. The first chapter introduces the Fuel Cells concept, focusing on the Solid Oxide Fuel Cell, defining the operating principles and the main components of a generic SOFC. The second chapter describes the model used by marking the difference between “First principle modeling” and the “Equivalent electrical circuits modeling”. In the same chapter, the SOFC studied is described in detail, highlighting the differences with the historically most used SOFCs. In the third chapter the model is validated by comparing the calculated results to the experimental ones. In order to validate the model, a fitting of data experimentally not obtainable (e.g. kinetic parameters) was made by means of the Optimization module available on COMSOL Multiphysics, Finally, in the last chapter, a sensitivity analysis for each parameter that could influence the quality of the simulation is conducted. It is important to notice that, most of these parameters are not experimentally accessible or easy to obtain. This shows that, the aid of modeling physical phenomena becomes more and more fundamental in the scientific field in order to speed up the process of technological innovation.

Chapter 1

Solid Oxide Fuel Cells

1.1 Fuel cells for energy production

Until today, most of the electrical energy is produced by using coal, oil, natural gas or nuclear energy. Only a relatively small percentage of the total energy is produced starting from renewables, such as solar energy or wind power. For instance, in 2018 renewable energy represented 18.9% of the energy produced in the EU [1]. Although renewable sources have the advantage of limiting pollution compared to the traditional energy sources mentioned above, these have the great disadvantage of working intermittently. Moreover, they also have a significant environmental impact which is often source of debate. The continuous increase of energy demand linked to the progressive consumption of fossil fuels, and the impossibility of filling this demand with renewable resources, has led many researchers to focus on fuel cells. A Fuel Cell is a device used to produce electricity and heat, as byproduct, from chemical energy at efficiencies greater than all the other conventional energy conversion technology (around 55-60%). The reason of this high efficiency is due to the fact that electrical energy is produced by directly converting the fuel, via electrochemical reactions, and therefore does not require the presence of thermal cycles and/or mechanical elements in movement [2,3]. This implies the intrinsic advantage of producing clean energy by avoiding the production of polluting agents, such as NO_x, SO_x and particulates. Another advantage of using fuel cells is that, unlike batteries that work for a limited period, they can continuously produce energy as long as they are fed with a source of fuel at the anode side and a source of oxygen (usually air) at the cathode side. Currently, there are six variations of fuel cells types that differ in construction materials, working agents and operating conditions [4]:

- *Alkaline Fuel Cells (AFC)* were one of the first developed FC technologies, characterized by an electrolyte consisting of potassium hydroxide and operating temperature range between 60°C and 120°C. Nowadays, they have reached a good level of technological maturity, especially in the military and space applications. The main disadvantage of AFCs is that they require extremely pure H_2 as feed because

they are extremely sensitive to carbon dioxide that can be found either in the fuel or air.

- *Proton Exchange Membrane Fuel Cells (PEMFC),* characterized by a polymer membrane with high proton conductivity as electrolyte and operating temperature range between 70°C and 100°C. The presence of the membrane requires the use of low temperatures to avoid its deterioration, however this leads to kinetic problems due to the high activation energies of the electrochemical reactions involved. To overcome this problem, it is necessary to use platinum as catalyst, making the cell too expensive.

- *Phosphoric Acid Fuel Cells (PAFC)* are characterized by a concentrated solution of phosphoric acid as electrolyte, and they operate in a temperature range between 150°C and 200°C. Platinum is used in PAFCs as well as an electrocatalyst in order to promote the reactions and increase their kinetics, because they are penalized by the low operating temperature. Developed in 60s they are nowadays used in stationary applications.

- *Molten Carbonate Fuel Cells (MCFC)* are characterized by a solution of molten alkaline carbonate as electrolyte. In order to maintain the alkaline carbonate in the liquid phase, the operating temperatures are above 650°C and this guarantees higher rates of reaction, avoiding the need of platinum as electrocatalyst and allowing the use of less expansive catalysts such as Nickel.

- *Direct Methanol Fuel Cells (DMFC)* can be considered as the evolution of the PEMFCs, they are still based on a polymer membrane as electrolyte but, in this case, the feed is composed of pure methanol instead of hydrogen at the anode and air, as always happens, at the cathode. DMFCs operate at temperatures between 80°C and 100°C and they are mainly used for portable applications, such as electronic devices.

- *Solid Oxide Fuel Cells (SOFC)* are the most studied and versatile cells. The operating temperatures are the highest compared to the other cell and they vary in a range between 600°C and 1000°C. SOFCs are characterized by an electrolyte made of ceramic material (like YSZ , Yttria stabilized Zirconia) and their use is suitable for the generation of electricity and cogeneration .

1.2 Solid Oxide Fuel Cells

Among all the fuel cells listed above, Solid Oxide Fuel Cells are considered a promising clean technology for power generation. Indeed, their operating conditions allow SOFCs to work with different type of feed, both fossil and renewable, and to use inexpensive electrocatalysts.

1.2.1 Working Principle

In a Solid Oxide Fuel Cell, the chemical energy content stored in a gaseous fuel is converted into electricity. The basic idea behind the functioning of a SOFC is that it is possible to derive energy from chemical reactions characterized by a Gibbs Free Energy lower than zero ($\Delta\tilde{G}_R < 0$), which are called "spontaneous reactions". It should be noted that, although a reaction can be thermodynamically favoured, it is not certain that it will occur with fast kinetics. In fact, thermodynamics does not give any information about the reaction kinetics and this means that spontaneous reaction could take hours, or even years, to occur. Undoubtedly, reactions limited by kinetics cannot find practical applications, so they need to be engineered, which practically means being catalysed. In a SOFC the reactions take place inside the porous electrodes, designed to promote the electrochemical reactions that occur inside the cell. However, in order for the reactions to take place, the fuel and the air supplied must be able to come into contact with the anode (also called *fuel electrode*) and cathode (also called *air electrode*) respectively, and to diffuse inside the pores of the electrode. This implies that a proper cell operation is not only dictated by electrochemistry but also by transport phenomena, therefore it is possible to highlight four key operating steps represented in Figure 1.1 [6]. The assembly of the anode, cathode and electrolyte layers is often called *membrane electrode assembly* (*MEA structure*).

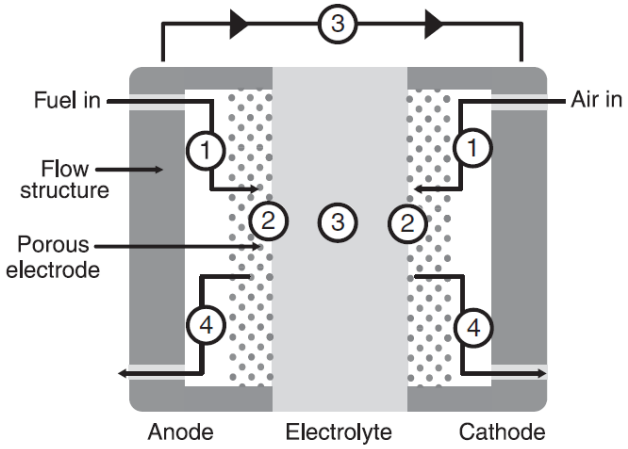

Figure 1.1. *Cross section of a planar SOFC with areas and steps involved [6]*

- *Step 1:* The first step is represented by the external and internal mass transport of the reactants. Fuel and air, which enter the respective gas chambers, move under the effect of a pressure gradient until they reach the external surface of the porous electrodes. At this point the reactants penetrate inside the pores of the electrodes and here they move by diffusion filling the voids due to the electrodes' porosity. It should be noted that the geometry of the gas chamber and of the cell itself considerably influences both the external and internal mass transfer, and this in turn determines an increase or decrease in the cell performances.

- *Step 2:* The second step involves the electrochemical reactions that take place inside the porous electrodes. As already mentioned, the cathode is in direct contact with the air while the anode is in direct contact with the fuel, typically pure H_2 or a mixture of H_2, CH_4, CO - assumed as fuel - and inert like H_2O, Ar or N_2. When we are in the presence of this gas mixture, in addition to the redox reactions between oxidants and reducing agents, both the reforming reaction of CH_4 to produce CO and H_2 (*Methane Steam Reforming, MSR*) and the oxidation reaction of CO to produce H_2 and CO_2 (*Water Gas Shift reaction, WGS*) can occur.
  Reactions can be summarized as in Table 1.1.

Table 1.1. Reactions that occur both anode and cathode side

Anode side reactions	Cathode side reaction
1. $H_2 + O^{2-} \leftrightarrow H_2O + 2e^-$	1. $O_2 + 4\,e^- \leftrightarrow 2\,O^{2-}$
2. $CO + O^{2-} \leftrightarrow CO_2 + 2e^-$	
3. $CH_4 + H_2O \leftrightarrow CO + 3H_2 (MSR)$	
4. $CO + H_2O \leftrightarrow CO_2 + H_2 (WGS)$	

The cathode is the electrode where oxygen reduction occurs with the consequent formation of oxygen ions O^{2-} by accepting $4e^-$ whereas, at the anode, considering pure hydrogen as fuel, H_2 reacts with the O^{2-} ions carried through the electrolyte from the cathode to the anode (*Step 3)* forming steam (H_2O).

- *Step 3:* The third step includes the transport of the electric and ionic charge. As seen in the previous step, oxidation reaction at the fuel electrode requires oxygen ions in order to take place and to produce the electrons, needed at the cathode to reduce the molecular oxygen. Therefore, a SOFC will be able to produce energy as long as ions and electrons are transported from where they are produced to where they are consumed [7]. The electrons are forced to pass through an external circuit that connects the anode and the cathode, while the transport of the oxygen ions from the

cathode to the anode takes place inside the MEA structure by means of the electrolyte, which is an excellent ionic conductor and electrical insulator. Notice that the transport of the electrons is rather easy to obtain, whereas the flow of oxygen ions that occurs under a chemical potential gradient, which forces the ions to pass from the cathode environment rich in oxygen ($p_{o2}^{C} \approx 0.21$ atm) to the anode ($p_{o2}^{A} \approx$1e-17 atm), is more difficult to obtain. Ions are indeed transported via *hopping mechanism,* which is less efficient than the electron transport mechanism, and it is based on the adsorption and desorption of the oxygen ions within the ionic vacancy present inside the electrolyte crystals [8].

- *Step 4:* The fourth step involves again the transport of species but in this case, unlike the first one, the reacted species are transported from the porous electrodes to the respective gas channels, and then dragged outside the cell. It should be noted that the air stream will deplete in oxygen while the fuel stream will deplete in reagent species such as hydrogen, methane, carbon monoxide or a mixture of these species.

1.2.2 Potentially Electrochemically Active Sites (PEAS)

As already mentioned, the electrochemical reactions take place inside the porous electrodes. However, it must be considered that not all the contact surface between solid and gas phase is electrochemically active, which means capable of causing reactions. Notice that the *MSR* and *WGS* reactions, when they occur, do not require the presence of active sites as they are catalysed by high working temperatures and, for this reason, they will occur both in the gas channel and inside the fuel electrode. It is therefore necessary to introduce the concept of *Potentially Electrochemically Active Sites (PEAS),* which is characterized by the presence of *Three Phase Boundaries (TPBs)* and/or *Double Phase Boundaries (DPBs)*.
In order to introduce the *PEAS* concept, it is important to clarify that the electrodes are typically composed of a mixture of solid powders, made of ionic and electrical conductive particles, which are subsequently subjected to a heat treatment called *sintering*, so that these powders form a single block, namely the electrode. The most common and historically used electrodes are called *CERMET* since they are composed of ceramic ionic conductor materials, such as YSZ or LSM, and metallic electrical conductor materials, such as Ni or Cu. Nowadays, the research of more performing materials has focused on new types of materials called *MIEC,* also known as *Mixed Ionic/Electronic Conductors*, which are capable of conducting both electrons and oxygen ions. The biggest advantage of these materials is that they can be used both pure or mixed with others solid powders in order to improve some

chemical and physical characteristics of the electrode; moreover, they strongly influence the presence and the spatial arrangement of the *PEAS*.

Depending on the materials used, two types of *PEAS* can be identified: *Three Phase Boundary* and *Double Phase Boundary*. By definition, the length of the *TPB* represents the active sites characterized by the coexistence of the gas phase, the solid ionic conducting phase and the electric conducting phase. This means that reactions can only occur in the active areas along the conducting paths, made by ionic/electric conductive particles, that completely cross the electrode from the top (interconnect) to the bottom (electrolyte). Notice that the *TPBs* can also be found in the case of composite electrodes mixed with *MIEC* particles. In the event that the electrode is composed, only or partially, by *MIEC* particles the *DPB* should also be evaluated as *PEAS*. The *DPB* is represented by the free surface of the *MIEC* particles in direct contact with the gas phase, and this implies that the electrochemical reactions can occur on the entire exposed surface of *MIEC* particles. Finally, for the sake of completeness, when the electrode is composed only of electrically conductive particles, the active sites will only be located along the contact line at the interface between the electrode particles and the electrolyte surface. Generally, this type of electrode is not widespread since it significantly limits the electrochemically active sites therefore the performance of the cell. By focusing for example on the cathode, it is possible to represent the *TPB* or the *DPB,* according to its composition, as represented in Figure 1.2 [7].

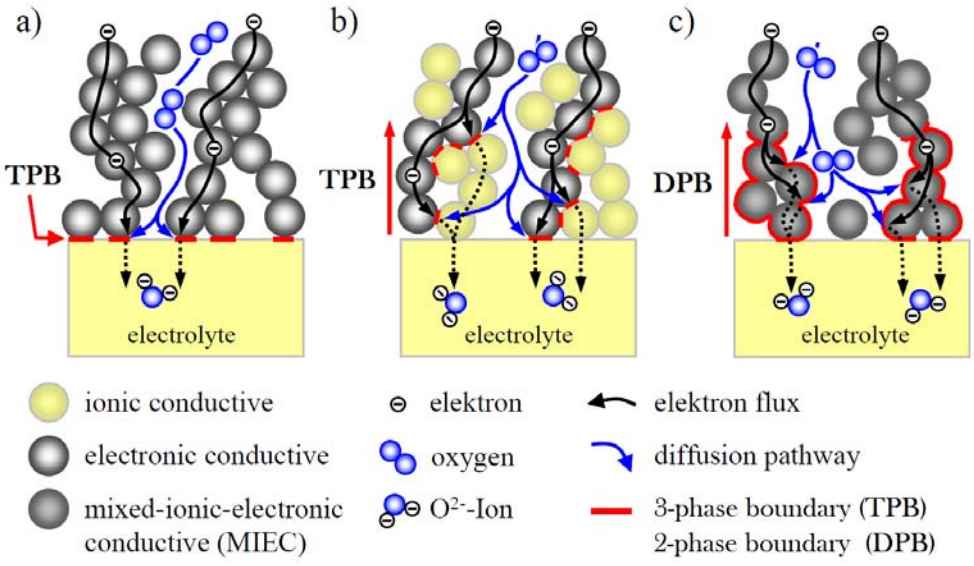

***Figure 1.2**. Representation of three possible PEAS in the air electrode: (a) Single phase electronic conductive electrode (b) Composite electrode without the presence of MIEC particles (c) Single phase MIEC electrode. [Adapted from 7]*

1.3 SOFC Characterization techniques

There are two ways that are commonly used to characterize a SOFC:

- *Polarization Curve (PC):* stationary analysis where the voltage of the cell is measured as a function of the current density [A/m^2] or the current [A] supplied.

- *Electrochemical Impedance Spectroscopy (EIS):* dynamic analysis in which the impedance of the cell is assessed and then charted in the Nyquist diagram.

1.3.1 Open Circuit Voltage and Nernst Equation

In a generic SOFC it is known that the reversible voltage potential, often indicated by *E*, represents the maximum thermodynamic potential that the cell can deliver, and it is a function of the Gibbs free energy, the number of electrons involved and the activity of the species. For the specific case of a SOFC fed with hydrogen and air, the global combustion reaction is:

$$H_2 + \frac{1}{2}\, O_2 \; = H_2O \tag{1.1}$$

Where the semi-reaction at the cathode is:

$$\frac{1}{2}\, O_{2(g)} + 2e^- \rightarrow O^{2-} \tag{1.2}$$

And the semi-reaction at the anode is:

$$H_{2(g)} + O^{2-} \rightarrow H_2O_{(g)} + 2e^- \tag{1.3}$$

For this particular reaction (1.1) the change in molar Gibbs free energy can be expressed as:

$$\Delta\tilde{G} = \Delta\tilde{G}^0 + RT \ln\left(\frac{a_{H_2O}}{a_{H_2}\, a_{O_2}^{0.5}}\right) \tag{1.4}$$

Where $\Delta\tilde{G}^0$ represents the molar Gibbs free energy at standard condition, and $a_i^{\nu_i}$ represents the activity for the generic species *i* elevated to its corresponding stoichiometric coefficient. Equation (1.4) is known as the van't Hoff isotherm and links the variation of molar Gibbs free energy to the activities of the species involved which, in the specific case of a reaction in the gas phase, can be replaced with the respective partial pressures.

By substituting in (1.4) the relation:

$$\Delta\tilde{G} = -z\,F\,E \tag{1.5}$$

that links the change in molar Gibbs free energy to the reversible voltage potential, where z is the number of electrons and F is the Faraday constant, we get the Nernst equation:

$$E_N = E^0 - \frac{RT}{zF}\ln\left(\frac{a_{H_2O}}{a_{H_2}\,a_{O_2}^{0.5}}\right) = E^0 - \frac{RT}{zF}\ln\left(\frac{p_{H_2O}}{p_{H_2}\,p_{O_2}^{0.5}}\right) \tag{1.6}$$

Where E^0 represents the potential at standard conditions. Note that this expression gives the voltage supplied by an ideal SOFC, E_N, which means at *Open Circuit Voltage (OCV)* conditions. This holds true only if there is no load connected to the cell, which means that the current supplied is zero.

1.3.2 Polarization Curve

When a load is applied to the cell, electrical current is drawn through the external electrical circuit causing a drop in the cell operating voltage which becomes smaller than the voltage evaluated by the Nernst equation: $V_{cell} < E_N$.

This is essentially due to the presence of irreversible processes, called *polarizations* or *overpotentials* and indicated with η, caused by different phenomena. When the cell voltage is plotted as a function of the current, or current density, supplied we get the Polarization Curve. In Figure 1.3, it is possible to see a typical example of a polarization curve in which the effects of the overpotentials are highlighted.

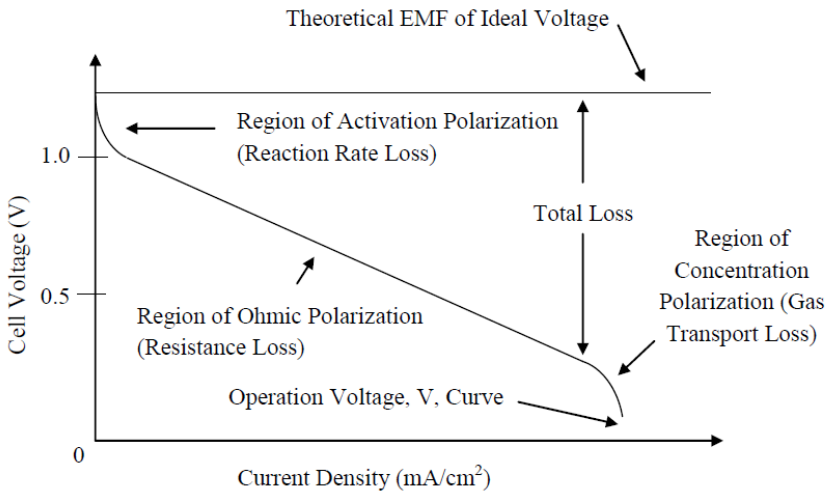

***Figure 1.3**. Polarization curve: Theoretical vs actual performance [9]*

It is possible to define three different type of overpotentials:

1. *Activation polarization losses:* at OCV condition the cell is at equilibrium so that, even though no current is delivered, the electrochemical reactions take place both at the anode and cathode with the same rate of reaction. Considering the cathodic current density, i_C, negative in sign, and the anodic current density, i_A, positive in sign, the net current density produced by the cell at OCV condition is zero [12]:

$$i_{net} = i_A - |i_C| = 0 \tag{1.7}$$

   In order to have a non-zero net current, it is necessary to perturb the system from its equilibrium condition, which results in a change in its ideal voltage ($V_{cell} \neq OCV$), overcoming the energy activation barrier characteristic for each reaction. A distinctive feature of electrochemical reactions is the ability to manipulate their activation barrier by varying the cell potential [6], and this happen because there is a direct link between Gibbs free energy and voltage changes, as in (1.5). In order to achieve a non-zero current density, an overpotential is needed and this is called *activation overpotential* or *activation polarization*. Notice that the contribution of the activation overpotentials is dominant for low temperature fuel cells whereas its effect is smaller for SOFCs. The activation polarization effect is visible in the polarization curve in the low current density area [2].

2. *Ohmic polarization losses:* they are due to the resistance offered by the electrodes and the electrolyte to the transport of charge, ionic and electrical. As the name suggests, Ohmic losses can be evaluated by the Ohm's law, $V = R\,I$, so the overvoltage at a given current supplied is proportional to the resistance offered to the charge flow. The same holds true for the ionic current.

3. *Concentration polarization losses:* they are caused by the mass transfer limitation from the bulk, i.e. the gas channels, to the PEAS inside the porous electrodes. Their effect becomes dominant in the high current density area of the polarization curve. When the concentration polarization is dominant, *Step 1* and *Step 4* (see as reference the paragraph *1.2.1*) are limiting the supply of the reacting species to the PEAS. This involves the formation of a concentration gradient inside the pores of the electrodes, with consequent drop of the partial pressure of the reacting species and an increase of the partial pressure of the reacted species. Since the voltage of the cell is also

linked to the activities of the reacting species, i.e. their partial pressure, this causes a voltage drop in the cell.

From Figure 1.3, it is clearly visible how voltage and current are tied together in a strongly non-linear way in the area in which activation overpotentials and concentration overpotentials are dominant, while it behaves like a resistor in the region of Ohmic overpotentials. Finally, this analysis can be carried out both in galvanostatic-mode, by progressively varying the voltage and measuring the current (or current density), or in potentiostatic-mode, by varying the current (or the current density) and measuring the voltage. The two methods are equivalent and return the same polarization curve when working under stationary conditions.

1.3.3 Electrochemical Impedance Spectroscopy

The Electrochemical Impedance Spectroscopy is considered as one of the best methods for studying the harmonic response of electrochemical systems. The concept of electrical resistance is well-known, and it describes the ability of a circuit to resists to the passage of current. This concept is described by the Ohm's law which binds voltage to current according to the relation $V = R\,I$. However, this definition in only applied to direct current systems (DC). For all the systems working with alternating current (AC), the concept of resistance is replaced by the concept of impedance, *Z*. Just like resistance, impedance measures the resistance offered to the flow of electrical current but, in this case, resistance is also a function of the frequency. Therefore, the impedance of an electrochemical system is estimated by applying a sinusoidal perturbation as input and measuring the response of the system in a wide range of frequencies. The EIS can be studied both in potentiostatic or galvanostatic mode as for polarization curve even though galvanostatic mode is usually preferred in SOFC applications [2]. Notice that, the behaviour of a SOFC is strongly non-linear and this makes difficult the interpretation of the EIS. To overcome this problem EIS is normally evaluated using a small excitation signal as input so that the response of the cell is pseudo-linear. The output response is characterized by the same input frequency but shifted in phase as seen in Figure 1.4.

To apply this technique, the cell is initially polarized and then, as previously stated, a small perturbation in the voltage, typically ranging from 5 to 50 mV, is applied. It should be noted that the typical voltage of a single cell stack is about 1 V, while the applied perturbation has about three order of magnitude of difference. Thereafter the frequency of the input perturbation is changed in a range between 10^{-2} Hz up to 10^{6} Hz and the impedance value is

evaluated at each frequency. In this way it is possible to highlight via EIS the different chemical and physical processes that occur inside the cell [13].

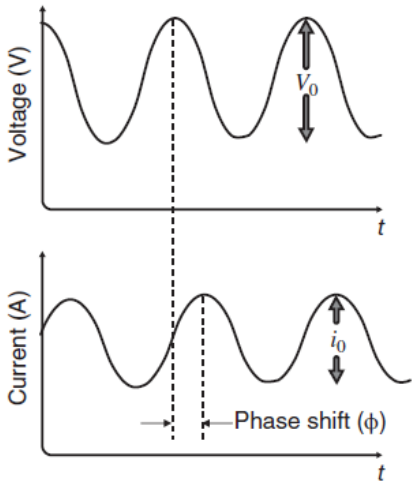

Figure 1.4. *Phase shift between tension and current in time domain [6]*

Mathematically, the evaluation of the impedance translates into applying the Ohm's law considering both voltage and current in sinusoidal form:

$$Z = \frac{V(t)}{I(t)} = \frac{V_0 \sin(\omega t)}{I_0 \sin(\omega t + \phi)} = Z_0 \frac{\sin(\omega t)}{\sin(\omega t + \phi)} \tag{1.8}$$

Where V_0, Z_0 and I_0 represent the amplitude of the voltage, impedance and current, ω the frequency and ϕ the phase shift.

The basic idea behind the EIS is to identify and weight the various processes taking place within a SOFC during operation, and to characterize them on the basis of their relaxation time. Relaxation time represents the time required by a process to return to its equilibrium state when excited by an external disturbance which, in this case, is represented by a sinusoidal change in the voltage or, rarely, the current. As can be seen from Figure 1.5, the charge transport phenomena are the fastest and they are characterized by low relaxation times and highlighted by high frequencies. The electrochemical reactions are characterized by relatively small relaxation times and they are perturbed at high-medium frequencies. Finally, mass transport phenomena are those with longer relaxation times and they are highlighted at low frequencies.

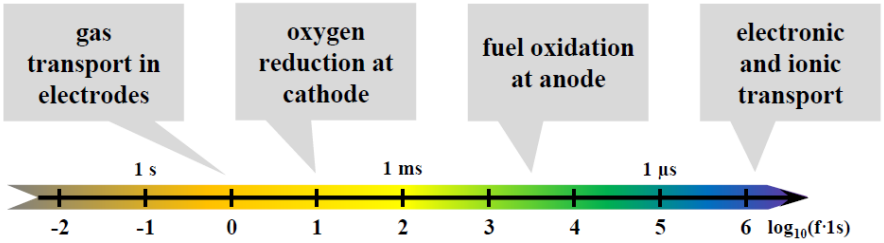

Figure 1.5. *Relaxation times of various phenomena as function of the frequency spectrum analysed in SOFC application. The typical frequency spectrum analysed - from* 10^{-2} *up to* 10^{6} *Hz - during SOFC characterization EIS [7].*

Once the values of the impedance are evaluated at each value of the frequency spectrum analysed, those values are plotted in the so-called Nyquist plot where it is possible to represents imaginary numbers. On the x-axis the real part of the impedance is represented while on the y-axis the imaginary part of the impedance, changed in sign, is plotted. Each point of the plot represents the value of the impedance at a certain frequency, and frequencies increase from the right to the left of the Nyquist plot. A generic example of Nyquist plot obtained through EIS analysis can be seen in Figure 1.6.

.

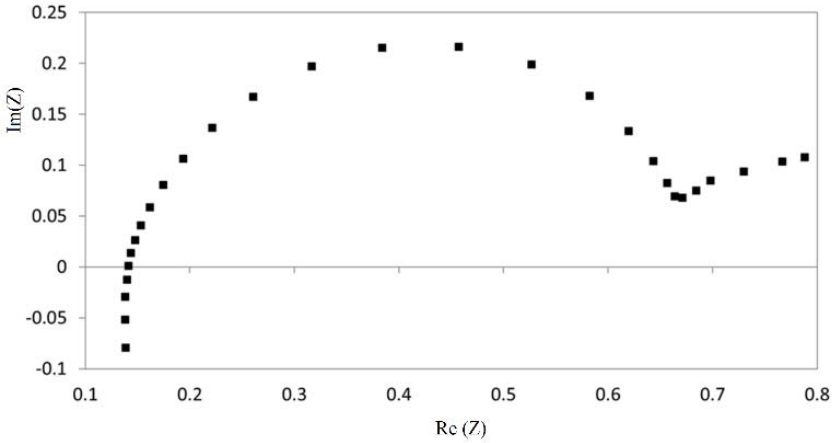

Figure 1.6*. General example of Nyquist plot used in EIS applications. Each point represents the value of impedance at a certain frequency. Notice that frequency increases from the right to the left of the plot. [14]*

A more detailed description and interpretation of EIS curves will be given in Chapter 3 and Chapter 4.

Chapter 2

Cell and Model Description

Solid Oxide Fuel Cells are complex devices where several physical and chemical phenomena occur simultaneously as seen in 1.2.1. Therefore, their description results in a highly nonlinear model described by a system of partial differential equations (PDE) and algebraic equations (AE). In order to solve this complex system, the commercial software COMSOL Multiphysics is used. The model is then validated, in the next chapter, through experimental data obtained from the laboratories of the Chemistry Department of the University of Padua. This chapter describes in detail the manufacturing of the SOFC studied, the construction of the model, the assumptions on which it is based, and the equations involved.

2.1 Equivalent circuits modeling vs First principle modeling

Among the two characterization methods described in the previous chapter, the electrochemical impedance spectroscopy is the most exhaustive and capable of providing a description of the chemical and physical phenomena occurring in a SOFC. EIS data are often interpreted in terms of *equivalent circuit model* (ECM). However, ECMs are not based on the actual description of the cell, hence the information that they can deliver on the processes involved is limited [15]. According to an ECM, a SOFC can be described by an RC circuit, i.e. composed of resistors and capacitors, or by an RLC circuit in which there is also the presence of inductors. This means that each circuit element should contain important information on the processes that influence the SOFC performance, although it is not always easy to identify the physical meaning of these circuit elements. In fact, while it is relatively easy to identify circuit elements for old-fashioned SOFCs, such as the YSZ-Ni/YSZ/LSM, the description of new SOFCs type using ECMs becomes much more difficult. ECMs are usually composed of a series of connected single impedance elements as well as other impedance functions, developed specifically for the SOFC description. The most common elements used in ECMs, their equations and a brief description of their meaning are represented in Table 2.1.

Table 2.1. Common circuit elements used in ECMs

Element	Equation	Description
Resistor	$Z_R(\omega) = R$	The resistor, which defines resistance, is often denoted by R and it has the unit of Ohm (Ω). It describes the non-ideal ionic and electronic charge transport.
Capacitor	$Z_C(\omega) = \frac{1}{j\omega C}$	The capacitor is denoted by the letter C and it has the unit of Farad (F). It usually describes the resistance to the charge transfer due to the Double layer Capacitance.
Inductor	$Z_L(\omega) = j\omega L$	The inductor, which defines inductance, is denoted by the letter L and it has the unit of Henry (H). It usually describes the effect of the external instruments on the measurements (parasitic inductances).
Warburg impedance	$Z_W(\omega) = \frac{1}{Y_0\sqrt{j\omega}}$	The Warburg impedance models the mass transport phenomena in a SOFC. There are several expressions, based on different assumptions, used to describe these phenomena. This definition is based on the assumption of semi-infinite diffusion layer. The Y_0 represents the diffusion admittance.

Figure 2.1 displays a typical example of ECM applied to a generic EIS measure. There are several commercial software, such as Zview, capable of identifying equivalent circuits and to model EIS curves. However, as already mentioned, the simplicity in fitting the experimental data with an ECM does not match the interpretation of the phenomena involved. In fact, a distinctive issue using ECMs is to attribute a physical meaning to each circuit element which, despite being present in the model, does not necessarily represent a real physical phenomenon. One way to overcome this problem is to describe SOFCs through a detailed model, that associates to each domain of the system equations capable of describing the chemical and physical phenomena that take place. These models are called *First Principle Models* (FPM) and in this thesis a FPM is developed.

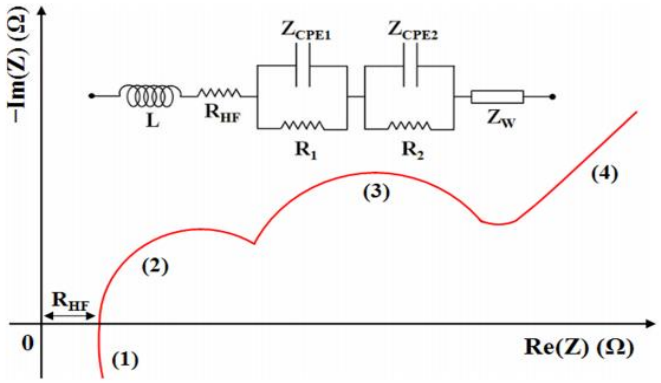

Figure 2.1. *General equivalent circuit model used to describe the EIS data reported in the red line*

FPMs allow to model each phenomenon involved - with physical and chemical laws - and, by varying the input data, it is possible to study how a SOFC behaves when changes occur. This particular study is called sensitivity analysis and will be covered in the Chapter 4. It should be noted that, although the use of FPMs allows for a better physical interpretation, these have the intrinsic disadvantage of requiring several input data, often unknown, and furthermore they are based on assumptions that may depart from reality. However, a certain degree of error is accepted considering that the calculated data are often very predictive, and they can help in developing SOFCs with higher performance. This concept can be extended to any scientific field where the FPM approach is used. In Figure 2.2 the operating principle of a FPM is described.

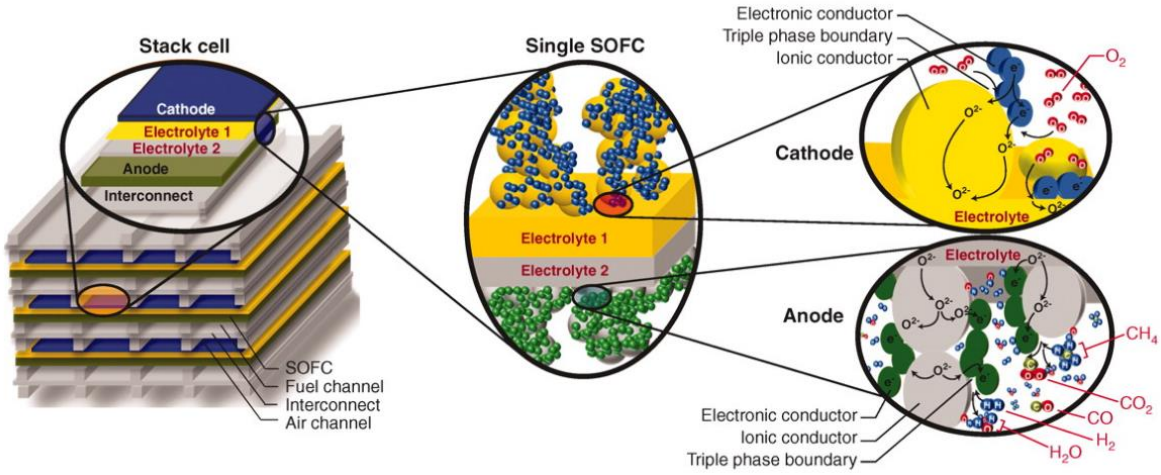

Figure 2.2*. Macroscale, mesoscale and microscale in a generic SOFC modeled with FPM approach.*

Starting from the macroscale, phenomena such as fluid dynamics and convective transport of species are described. Then, at mesoscale, the diffusion of the gases within the porous domains is described, considering the geometry and the construction features of the

electrodes. Finally, at the microscale, reactive phenomena are modeled considering that electrochemistry is directly connected to the presence of active sites (PEAS).

2.2 Experimental SOFC: Components and Design

Solid Oxide Fuel Cells, like all the other fuel cells, are composed by electrodes, anode and cathode, and the electrolyte [5]. A more detailed description of the SOFC components, materials involved and preparation techniques specifically for the SOFC studied in this thesis is described as follows. A distinctive feature of this SOFC is that it uses different materials that the typical ones: YSZ and LSM. Furthermore, the manufacturing of the electrodes occurs according to two different methods, leading to an "impregnated anode" and a "composite cathode".

2.2.1 MEA Structure of the studied SOFC

- ***Electrolyte***

In a SOFC the electrolyte has the task of separating the gases supplied to prevent the direct combustion of fuel and oxidant, and to ensure that the difference in chemical potential between the two electrodes remains as high as possible in order to force the passage of the oxygen ions from the cathode to the anode. As stated in chapter 1, there is a great difference in the partial pressure of oxygen between the oxidizing and reducing zone of the SOFC, and this difference represents the driving force for the transport of oxygen ions. Notice that, if this transport did not take place, the cell would cease to function. In Figure 2.3 [7] is clearly visible the scheme of a generic SOFC with the respective components, that will be analysed in this paragraph. Moreover, the difference in oxygen concentration in the two compartments, separated by the electrolyte, is well highlighted.
Therefore, the electrolyte must be: an excellent ion conductor, coupled with a very low electronic conductivity in order to force the electric current to pass through the external circuit avoiding current leakage, manufactured in such a way as to be as gas tight as possible, chemically stable as it is exposed both to strongly reducing and oxidizing environments and, characterized by a thermal expansion coefficient similar to that of electrodes to overcome mechanical stress. The historically most used and studied electrolyte in SOFC applications is the Yttrium Stabilized Zinrconium (YSZ), characterized by high ionic conductivity at a temperature above 750°C and good chemical stability [7,9].

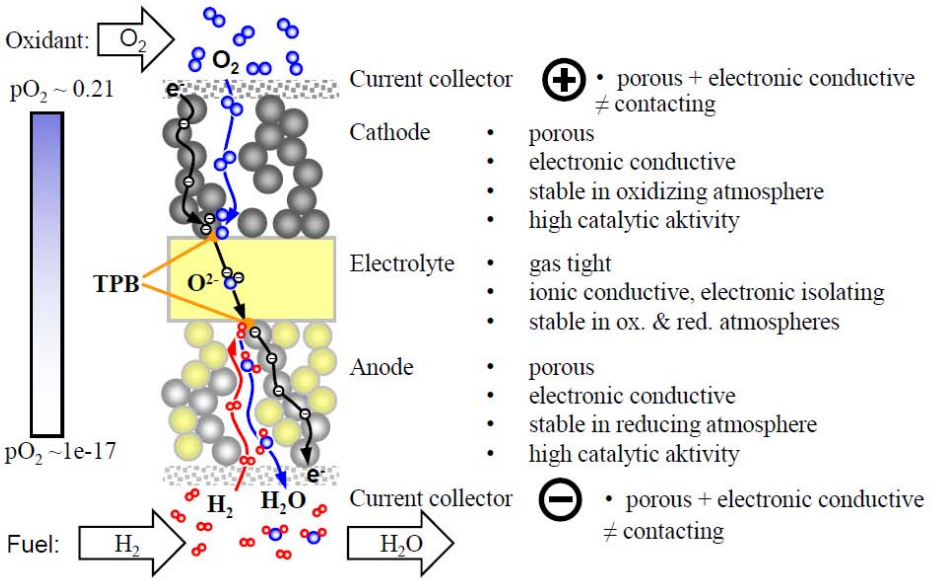

Figure 2.3. *MEA structure with its chemical-physical characteristics. The cathode represents the positive electrode while the anode represents the negative electrode. On the left the difference in oxygen partial pressure due to the presence of the solid impermeable electrolyte. [Adapted from 7]*

However, the continuous research of new promising materials, in order to produce Low-Temperature working SOFC (LT-SOFC) - operating lower than 650°C - or Intermediate-Temperature working SOFC (IT-SOFC) - operating range 600-800°C - has caused a decreasing interest on the YSZ during recent years.

In this thesis the electrolyte used is the *Gadolinium doped Ceria* (*CGO*), a solid ceramic material characterized by a cubic crystal structure in which the oxygen vacancies, produced during the doping process of Gadolinium into Ceria, give this material a high ionic conductivity at intermediate temperatures (500-700°C). Although these temperatures may seem particularly high, it must be remembered that a classical SOFC with YSZ as electrolyte requires operating temperatures ranging from 750 up to 1000°C. The electrolyte used for the purpose of the thesis is manufactured starting from the pure CGO powders, purchased from FuelCellMaterials. They are first pressed, giving them a well-defined shape and compactness, and then subjected to a sintering heat treatment at 1500°C for 6 hours. At the end of the process there will be a 1 mm thick electrolyte disc which, as explained in the next paragraph, also has the function of providing mechanical resistance to the cell.

- ***Cathode***

The cathode is the electrode where oxygen reduction takes place, with the consequent formation of oxygen ions O^{2-} . This implies that the cathode must be designed to have high catalytic activity, high electrical and ionic conductivity, high chemical stability (considering the strongly oxidizing environment), a good degree of porosity (to allow gases to permeate) and finally a thermal expansion coefficient similar to the other components present in the cell (anode and electrolyte). Although the research of new promising and performing materials often focuses only on their ionic and electrical conductivity, the operating temperatures of the SOFCs do not allow to neglect the thermal expansion of the material used, making the thermal expansion coefficient a key design parameter. Notice that, at 600°C up to 1000°C, typical temperature operating range, if the materials used have different thermal expansion coefficients, cracking of both the electrodes and/or electrolyte with the consequent malfunction of the cell may occur due to mechanical stress. A very common material used in cathode manufacturing is the Strontium Stabilized Lanthanum Manganite (LSM). However, nowadays, materials that expand the TPB such as MIEC materials are preferred.
In this thesis, the SOFC used is characterized by a cathode composed of *Lanthanum Strontium Cobalt Ferrite* (*LSCF*) and *Gadolinium doped Ceria* (*CGO*) powders. This powders mixture was purchased from the *Sigma-Aldrich* and is composed of 50%wt of LSCF and 50%wt of CGO. Notice that the LSCF is a MIEC material, while the CGO is a ceramic material. The cathode deposition process starts with the creation of an ink, composed by the aforementioned powders to which a binder is added, the Alpha Terpineol, at 50%wt of the total mass plus a 3%wt of Carbon soot. The latter is a pore former which means a compound that, during the sintering process, burns favouring the presence of voids inside the electrode increasing its porosity. Once the ink has been created, it is necessary to adjust its viscosity because an excessively viscous ink is difficult to handle while, an excessively low viscosity ink leads to an electrode with poor performance. In order to obtain the optimal viscosity, 2-3 drops of a thinner, based on Alpha Terpineol, are then added. After the ink preparation is complete, it is deposited on the electrolyte surface by means of a 30 μm thick mask which allows to create an electrode with roughly that thickness. This deposition method is called *Tape Casting*.

- ***Anode***

The anode is the porous electrode in which the oxidation of the fuel takes place. Therefore, it is characterized by a good catalytic activity, due to the presence of metals, high electrical

conductivity, acceptable ionic conductivity and high chemical stability to resist the reducing conditions. As seen for the cathode, properties such as porosity and thermal expansion coefficient are key parameters to manufacture a promising electrode. In order to have all the characteristics mentioned above, the anode is often a composite electrode called cermet, which means composed of ceramic material and metals. The solid ceramic phase gives the ionic conductivity to the electrode while the solid metallic phase gives the electrical conductivity and, in addition, acts as an electrocatalyst. There are several cermets studied in the literature but, historically, the most used one is the Ni/YSZ electrode composed precisely of a metal, Ni, and ceramic material, YSZ. Although this anode is very active, due the presence of Ni, it suffers the deactivation of active sites with the consequent loss of performance. In order to avoid this problem Ni is often replaced with other metals, preferably not noble metals to keep costs down, capable of being more stable and performing over time. In this thesis the anode used is also a cermet, composed of CGO and Cu. The manufacturing process is highly different from the one seen at the cathode as this is an impregnated electrode. The main feature of impregnated electrodes consists in the fact that these are characterized by a backbone of micrometric particles, on which a coating of nanometric particles is applied. For this specific anode, the backbone is composed of CGO micrometric particles covered with Cu nanometric particles. Impregnated electrodes have the intrinsic advantage of greatly increasing the length of the TPB thus increasing the PEAS, with an increase of the performance of the cell. This is mainly due to the difference between the average diameters of CGO and Cu particles (about 1/10), an advantage that is not found in typical cermet prepared from ionic and electrical solid phase powders with similar mean diameter.

The electrode production process is called *Impregnation Method*. The manufacturing of the Cu-CGO electrode starts with mixing in a beaker water, CGO powders (the same used for the electrolyte), Copper Nitrate which is soluble in water and Nitric acid. Once the precursors are dissolved in the concentrated nitric acid solution, a complexing agent such as Citric acid is added. Citric acid is a weak carboxylic acid able to promote the formation of a network among the precursors involved. The resulting solution is characterized by pH∼1 therefore a change in pH is necessary to complete the dissociation of citric acid. In order to increase the pH, ammonium hydroxide is added until a pH=8 is reached. The choice of this pH value is not arbitrary, but it is the result of a previous study carried out by researchers from the Chemistry Department of Padua [10]. The mixture is then subjected to an evaporation process of the water until a gel is formed, which is subsequently heat treated in order to precipitate Copper Oxide crystallites, CuO. Once the cell is under operation, copper oxide gets reduced forming metallic copper crystals by means of the hydrogen stream fed at the anode side.

Notice that anode and cathode are sintered on the electrolyte at different temperatures and the process requires two days of work. First, the cathode is deposited on the electrolyte via sintering at 1200°C and then, 24 hours after this process, the anode deposition process takes place at a temperature of 1050°C. The difference in temperature is due to the presence of Cu in the anode which, at a temperature above 1050°C, would tend to soften excessively or even melt ($T_{m,Cu}$ =1085°C) forming a single block of copper which would completely compromise the functionality of the electrode itself. Finally, both electrodes are covered with a gold paste in order to connect the SOFC to and external load through electric cables.

2.2.2 Common and adopted SOFC design

There are several designs commonly used in SOFC production industry. In Table 2.2 are summarized the most common single stack SOFC design, employed both on industrial and laboratory scale [9,11,26].

Table 2.2. Single stack SOFC design [9,11,26]

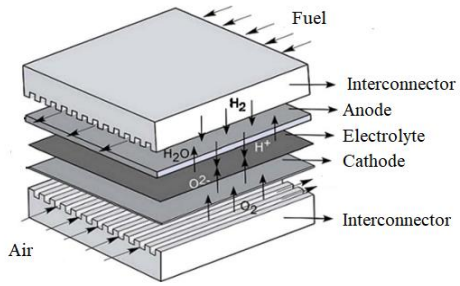	*Conventional planar SOFC*
	*Button planar SOFC (Anode supported)*
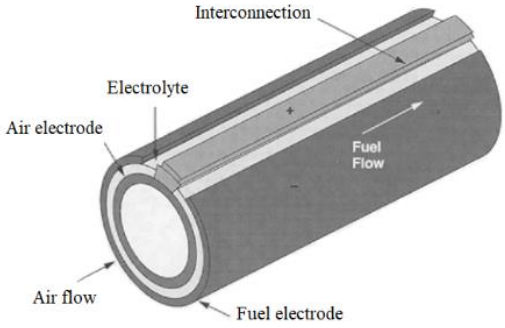	*Tubular SOFC*

Each SOFC in the table represents a single stack which, in real applications, is repeated a certain amount of times by connecting the single stack in series so that the desired voltage

and power is achieved. As regards the study carried out in this thesis, a single stack button planar SOFC is studied. Notice that, among the button SOFCs there are three variants according to the component of the MEA structure which gives mechanical strength to the cell, which practically means a greater thickness. We can therefore deal with "electrolyte supported cells", "anode supported cells" and "cathode supported cells". The choice among electrolyte/anode/cathode supported cell also influences the performance of the cell: generally, the latest generation SOFCs are anode/cathode supported. However, the cell used in this thesis is electrolyte supported with the advantage of decreasing the thickness of the electrodes, allowing for an immediate supply of the reactive species to the respective PEAS, but with the intrinsic disadvantage of increasing the Ohmic resistance of the electrolyte layer towards the ions transport. The single stack button SOFC used is shown in Figure 2.4.

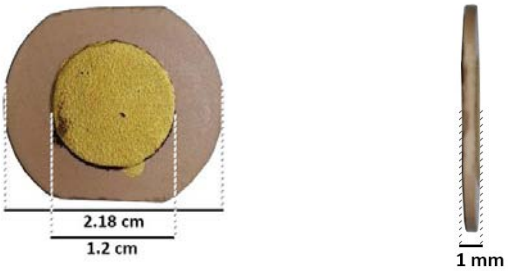

Figure 2.4. *Single stack button SOFC modeled in this work (Anode: Cu-CGO; Electrolyte: CGO; Cathode: LSCF-CGO). On the left the top view, on the right the thickness of the electrolyte.*

2.3 Computational domains and Meshing

As mentioned, the studied SOFC is modeled by means of COMSOL Multiphysics. Through this software the simulation of any physical phenomenon is obtained using a numerical technique called Finite Element Method (FEM). In order to run the simulation, it is first required to define the geometry of the system by identifying the various domains. Subsequently, in order to apply the FEM technique, a mesh consisting of many small elements that together form the shape of the modeled geometry needs to be created. Therefore, each domain is characterized by *n*-elements and the equations are solved simultaneously in each of these until a global solution is reached [16].

2.3.1 Geometry

In the previous paragraph the shape and the design of the SOFC studied is defined. In order to be characterized, the cell is locked between two hollow double-tubes with the function of blocking it and guiding the gases fed to the cell and the outwards. In Figure 2.5 it is possible

to see a simplified sketch of the cell in which the internal feeding tubes and the motion of the gases are highlighted.

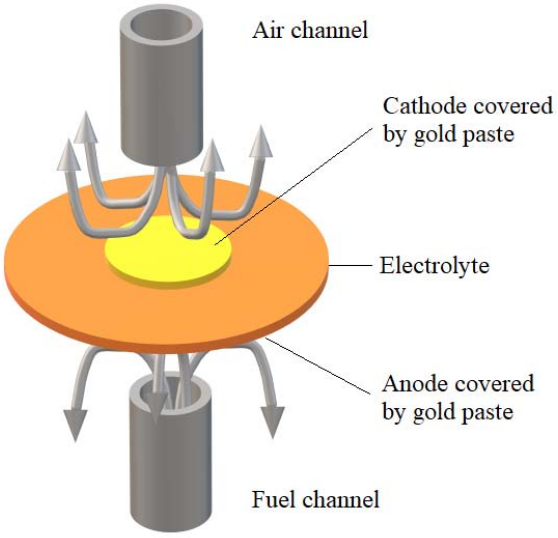

Figure 2.5. *Sketch of the SOFC; the gases are fed through the internal tube of the double-tube. The external tube, blocking the electrolyte, conveys the reacted and unreacted gases to the outside.*

In order to bring the SOFC to the operating working conditions (T=650÷660°C and P=1atm), it is first inserted inside an electric oven, and then connected to the supply gas tanks and to the external electrical circuit to carry out the measurement (PC and EIS). In Figure 2.6, the electrical oven used with the cables of the electrical circuit connected to the cell is shown.

Figure 2.6*. Electrical oven used to reach the operating temperature of 650°C.*

Since the geometry of the system is axial-symmetric, it is possible to analyse the system by representing a single two-dimensional (2-D) section as in Figure 2.7. The results are then extended to the whole geometry, by rotating by 360° the section with respect to its symmetry axis. The geometrical parameters of the gas channels and SOFC are reported in Table 2.3.

Table 2.3. Geometrical details of the simulated SOFC

Anode/Cathode/Gold paste diameter	*Electrolyte diameter*	*Anode/Cathode thickness*	*Electrolyte thickness*	*Gold paste thickness*	*Double tube Internal Diameters*
12 mm	21.8 mm	30 μm	1 mm	60[#] μm	10.3 mm 17 mm

Reasonable value assumed in this work. The real value is difficult to evaluate because, by cutting the cell to make a SEM analysis, the gold paste detaches itself.

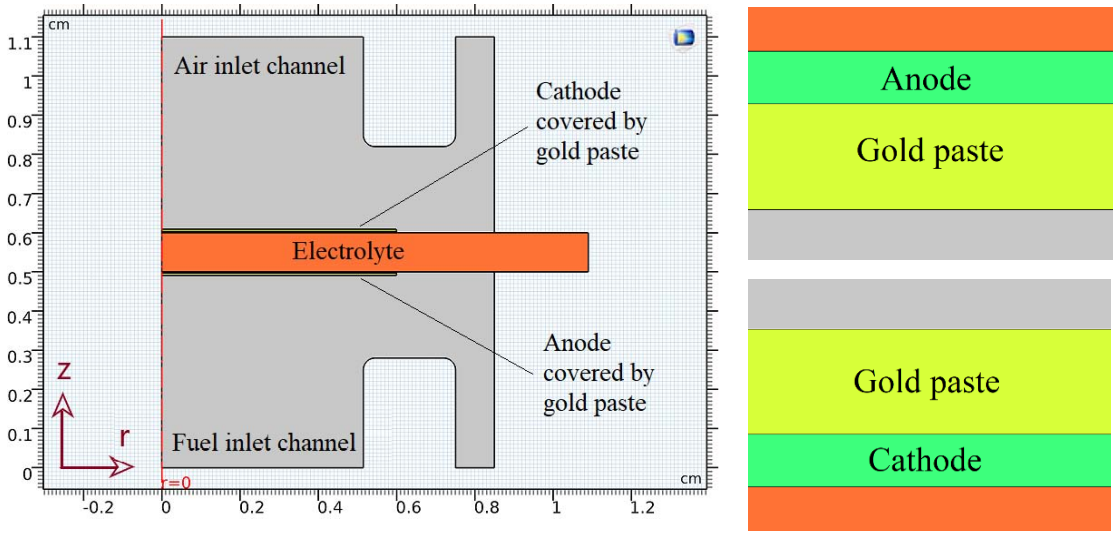

a) *b)*

Figure 2.7. *a) 2-D axial symmetric geometry used in this simulation. b) Details of the active layers and gold paste (different view adopted for visualization purposes).*

2.3.2 Adopted Mesh

The quality of a model is often influenced by the quality and number of the meshes used. A proper mesh must fulfil two basic rules: no void regions in the computational domain and no overlapping mesh elements. Moreover, mesh should also aim for the following three factors [17]:

1. High quality
2. Sufficient resolution for the desired accuracy
3. Low computational cost

In this study there are several domains characterized by different physical phenomena. Therefore, the use of different meshes is needed in order to properly highlight gradients in the involved variables. In the gas channels, the fluid dynamics must be described. Typically, fluid dynamics is described by the so called "Free triangular meshes", capable of accurately representing the fluid flow with a relatively low computational cost. The velocity, pressure and composition gradients within the gas channels are then described using these meshes. For what concerns the porous electrodes, the electrolyte and the gold paste, the *r*-gradients in these domains are negligible compared to the *z*-gradients. For that reason, the use of "Mapped rectangular meshes" is preferred allowing to describe gradients of the variables studied (such as concentration and charge exchange). Meshes used are shown in Figure 2.8.

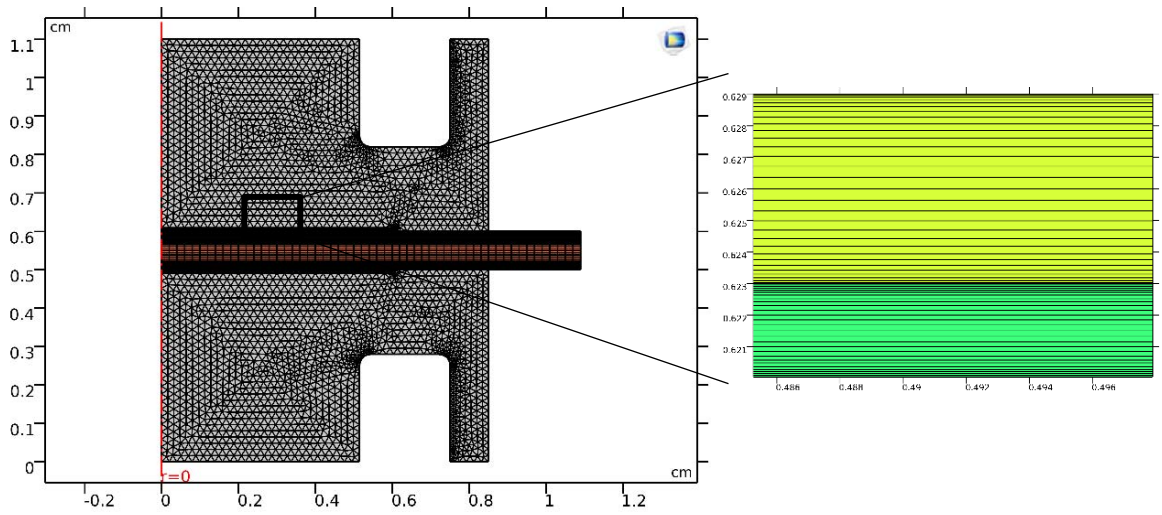

Figure 2.8. *On the left the meshing of the entire geometry. On the right the meshing of the gold paste (yellow) and electrode (green).*

Complete mesh consists of 11832 domain elements and 842 boundary elements.
Sensitivity analysis on the number of domains was carried out by showing that, intensifying the number of domains (i.e. tripling them) used in the mesh does not affect the result significantly enough to justify an increase in computational effort. The effect of the change in the number of domain elements is shown in Figure 2.9.

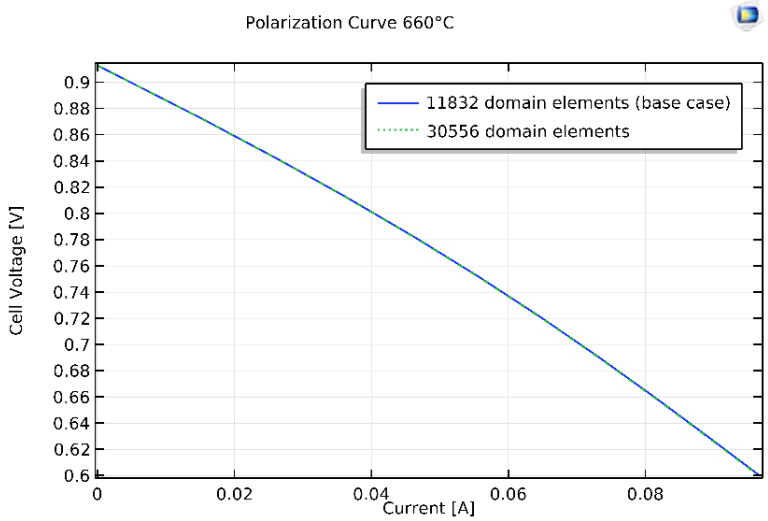

Figure 2.9. *Effect of an increase in the number of domain elements on a calculated polarization curve compared with the base case.*

As it can be seen, the two curves perfectly overlap. Therefore, the number of domain elements used to describe the system is appropriate.

2.4 Model assumptions, equations and effective properties

2.4.1 Assumptions

Before delving into the details of the equations, algebraic and differentials, which describe the SOFC studied, the assumptions on which the model is based are listed.

- *Isothermal system.* As seen in Figure 2.6, the cell in inserted in the electric oven to reach its working temperature. Although the global combustion reaction of hydrogen is an exothermic reaction, the low conversion of the reacting species leads to the simplification of considering a zero-temperature gradient. In the literature several studies show the negligibility of temperature gradients [18,19]. Therefore, it was decided to focus on the phenomena involved neglecting the effect of

temperature gradients. This implies not considering energy balance equations in the model.

- *Ideal gas law.* Considering the operating condition of the SOFC modeled in this work - high temperature, ambient pressure and low molecular weight of the species involved - it is reasonable to consider the gas phase as an ideal gas mixture. This implies the use of the ideal gas law, $PV = nRT$.

- *Porous domains modeled as a pseudo-continuous phase.* Both the electrodes and the gold paste are studied as a continuous and isotropic pseudo-phase. This means that these domains are globally characterized by their permeability, which is evaluated by using porosity, tortuosity and average diameter of the powders that constitute them. In this way it is also possible to evaluate other average properties for these domains, called "effective properties", which translates into finding effective ionic and electrical conductivities or an effective distribution of the active sites (effective TPBs/DPBs). In the following paragraph, these effective properties are assessed through specific models based on "Percolation Theory".

- *Degradation effect neglected.* Both mechanical and catalytic degradation can occur in a cell. In the first case, the high temperatures involved can lead to fractures in materials, compromising their functioning. In the second case, the number of active sites decreases. This can be caused by the high temperatures (sintering process) and by the presence in the feed of compounds that poison the catalyst (poisoning effect).

2.4.2 COMSOL modules (Physics)

When creating a simulation in COMSOL Multiphysics, a fundamental step required by the software in order to launch the simulation is to define the "*Physics*". This step is mandatory. Several physics may be involved, and this essentially depends on the complexity of the phenomena described. The following modules have been used in this simulation.

Free and Porous Media Flow module. In order to evaluate the fluid velocity and pressure field within the SOFC, this module has been added. It finds application in all domains (gas channels, porous electrodes and gold paste layers) except in the electrolyte domain. The latter is in fact composed of a dense ceramic layer and it does not allow the flow of the gaseous species. Porous domains and free domains differ in the equations that characterize them. While in a porous domain diffusive phenomena predominate, in a free domain

convection governs the fluid motion. This translates into the choice of Brinkman's equation to describe the fluid dynamics in porous domains and the Navier-Stokes equations to characterize free domains. Notice that each module requires input data; in this case the required inputs are:

- Fluid density
- Fluid viscosity
- Inlet and outlet pressure
- Porosity of porous domains
- Permeability of porous domains

Transport of Concentrated Species. This module is used to study concentration gradients of gaseous and liquid mixtures, where the species concentrations are of the same order of magnitude and none of the species can be identified as a solvent. In this case, properties of the mixture depend on the composition, and the molecular and ionic interactions between all species need to be considered. The physics interface includes models for multicomponent diffusion, where the diffusive driving force of each species depends on the mixture composition, temperature and pressure. Transport through convection, diffusion and migration in an electric field can be included. There are several available diffusion models on COMSOL Multiphysics such as the Maxwell-Stefan diffusion model, the Mixture average diffusion model or the Fick diffusion model. In this thesis the Maxwell-Stefan model has been used: it represents the most detailed diffusion model, but it is also the most computationally expansive. As for the previous module, the transport of concentrated species module also finds applications in all domains except for the electrolyte. The required inputs are:

- Temperature
- Pressure
- Feed inlet flowrates (anode and cathode side)
- Binary diffusion coefficient matrix
- Mean pore diameter

Secondary Current Distribution. This module accounts for the electronic and ionic charge balance in the anode, cathode, electrolyte and gold paste layers. It also accounts for the relation between charge transfer and overpotentials by means of the Butler-Volmer kinetic expression. Moreover, the Butler-Volmer equation is used to model electrochemical reactions providing a global description of these. It is called Secondary Current Distribution

because, as for the Primary Current Distribution, the electrolyte current is measured with the Ohm's law but it also accounts for the electrochemical reactions within the porous electrodes [47]. The input data required are:

- Ionic and electronic effective conductivities
- TPB length per unit volume and DPB
- Kinetic expression (often a modified Butler-Volmer as in this thesis)

2.4.3 Modeling equations

The equations that characterize each of the modules listed above are now described in detail [20,23].

Free and Porous Media Flow module

The description of the velocity field depends on the flowrates involved. Since the inlet feed flow, both anode and cathode side, is 100 sccm, the calculated maximum inlet velocity is about 0.12 m/s. Such low velocity implies a laminar regime. The laminar flow module in COMSOL Multiphysics uses the Navier-Stokes equation in order to describe the momentum balance for the gaseous species, assumed to be compressible, at anode and cathode side:

$$\rho(\nabla \mathrm{u})\mathrm{u} = \nabla\left[-\mathrm{PI} + \mu\left(\nabla \mathrm{u} + (\nabla \mathrm{u})^{\mathrm{T}} - \frac{2}{3}\mu(\nabla \mathrm{u})\mathrm{I}\right)\right] \tag{2.1}$$

At steady-state the Navier-Stokes are solved in conjunction with the continuity equation:

$$\nabla(\rho u) = 0 \tag{2.2}$$

Since the Free and Porous media module is also used to evaluate the fluid dynamics of the gas phase within the porous domains, an extended Navier-Stokes equation, called Brinkman equation, is used only within anode, cathode and gold interconnect layers. This equation accounts for the porosity and the permeability of the aforementioned domains:

$$\frac{\rho}{\varepsilon}(\nabla u)\frac{u}{\varepsilon} = \nabla\left[-\mathrm{PI} + \frac{\mu}{\varepsilon}\left(\nabla \mathrm{u} + (\nabla \mathrm{u})^{\mathrm{T}} - \frac{2\mu}{3\varepsilon}(\nabla \mathrm{u})\mathrm{I}\right)\right] - \left(\frac{\mu}{\mathrm{K}} + \beta_F|u| + \frac{Q_{br}}{\varepsilon^2}\right) \tag{2.3}$$

where ρ represents the fluid density $[kg/m^3]$ evaluated by means of the ideal gas law, u is the velocity vector $[m/s]$, P is the pressure $[Pa]$, I is the identity matrix, μ is the dynamic

viscosity $[Pa \cdot s]$, K is the permeability $[m^2]$, ε the porosity of the porous matrix. Notice that in the Brinkman equation $\beta_F[Pa \cdot s]$ represents an effective value for the dynamic viscosity of the gas phase within the porous domain while $Q_{br}[kg/(m^2 \cdot s)]$ represents an additional species source term that takes into account both production and consumption of gaseous species in the reactive layers. Therefore, since the density and velocity are no longer constant in the porous domains, the continuity equation becomes:

$$\nabla(\rho u) = Q_{br} \tag{2.4}$$

In Table 2.4 the equations and operating parameters used to evaluate the calculated parameters required in this module.

Table 2.4. Parameters and equation used in Free and Porous Media Flow module

Parameters and Data	***Value or Expression***	***Reference***
Inlet anode flowrate	$100\ sccm\ (48.5\%\ H_2, 48.5\%\ Ar, 3\%H_2O)$	This work
Inlet cathode flowrate	$100\ sccm\ (21\%\ O_2, 79\%\ N_2)$	This work
T	$650 \div 660°C$	This work
P	$1\ atm$	This work
ρ	$PV = nRT$	
μ_i	$\mu_i = \sum_{k=0}^{6} b_{i,k} \frac{T(K)}{1000}$	[21]##
μ_{mix}	$\mu_{mix} = \sum x_i \cdot \mu_i$	[21]
$\mathrm{K}_{A/C}$	$\mathrm{K}_{A/C} = \frac{D_p^2}{150} \cdot \left(\frac{\varepsilon_{A/C}^3}{\left(1 - \varepsilon_{A/C}\right)^2} \right)$	[22]#
D_p	$D_p = \frac{3}{2} \frac{d_p(1-\varepsilon)}{\varepsilon}$	[22]#
ε_A	0.3	This work*
ε_C	0.2	This work*
ε_{Au}	0.25	This work*

*Reasonable values found in literature. The difference in porosity between the anode and cathode depends on the different manufacturing techniques already discussed. The effect of variation of these values is assessed in Chapter 4.

[#]These data will be evaluated using the percolation theory.

[##]Data used for the polynomial equation in Appendix.

A=Anode ; C=Cathode ; Au=gold paste; *i* =generic gaseous species; D_p= mean particle diameter; d_p= mean pore diameter.

Transport of Concentrated Species module

The mass conservation law states that mass cannot be created nor destroyed, and it is the governing equation for mass transfer phenomena that happen within the SOFC. For what concerns both anode and cathode gas channels, diffusion and convection in a free space are considered. However, the model also accounts for restrictions in porous domains by considering their microstructural features. This is done by means of the porosity, tortuosity and Knudsen diffusion. The steady state mass balance can be expressed as:

$$\nabla J_i + \rho(\nabla \cdot u) w_i = S_i \tag{2.5}$$

where J_i is the mass flux of the generic species *i* $[kg/(m^2 s)]$, S_i is the mass rate of production/consumption of species *i* due to the electrochemical reaction $[kg/(m^3 s)]$, ρ is the density $[kg/m^3]$ and w_i is the mass fraction of the generic species *i.* Generally, to describe concentration gradients in SOFC's porous domains, the Dusty-Gas model is considered the best approximation model. This is a transport model that describes the flow of fluid mixtures through porous media. Its name depends on the assumption for which, in a multicomponent mixture of *n* species, the porous medium is described as an additional (*n+1*)-th component of the mixture, consisting of a "dust particles" fixed in the space. Even though the Dusty-Gas model is considered the best approximation model to simulate mass transfer phenomena in a SOFC [2], when operating at low current feed and high reactant concentration, the less computationally expensive Stefan-Maxwell model is preferred. Therefore, the Stefan-Maxwell model is implemented in this thesis. Furthermore, notice that the Dusty-Gas model is not directly implemented in COMSOL Multiphysics. When using the Stefan-Maxwell diffusion model, the mass flux vector can be written as:

$$J_i = -\sum_{j=1}^{n-1} \rho \, D_{ij}^{eff} \, \nabla w_j \tag{2.6}$$

where D_{ij}^{eff} is the effective binary diffusion coefficient $[m^2/s]$. Notice that in porous media diffusion is often described by the Bosanquet equation that considers both the molecular

Fuller diffusion (particle-particle collisions), and the Kndudsen diffusion (particle-wall collisions) which is function of the mean pore diameter. The Bosanquet equation allows to define an effective diffusion coefficient used for both the anode and cathode domain. Effective properties define an average value, which means not local, for a certain variable, and these are used to describe porous domains as a pseudo-continuous phases. For what concerns the gold paste layer, since the mean pore diameter is not known or assessable via Percolation Theory, an effective diffusion coefficient is evaluated by using the Bruggerman model built in COMSOL Multiphysics. In Chapter 4 is then assessed the effect of a change in the gold paste effective diffusion coefficient on the system. Finally, in the gas channels the binary diffusion coefficients are evaluated through the Fuller equation. In Table 2.5 the equations used to evaluate the binary diffusion coefficients in different domains are listed.

Table 2.5. Binary diffusion coefficients equations

Parameters	***Expression***	***Reference***
Fuller binary diffusion coefficient (Gas channels)	$D_{ij} = \frac{1.43 \cdot 10^{-7}\, T^{1.75}}{P\left[v_i^{\frac{1}{3}} + v_j^{\frac{1}{3}}\right]\left(2\left(\frac{1}{MW_i} + \frac{1}{MW_j}\right)^{-1}\right)^{0.5}}$	[23,21]#
Knudsen binary diffusion coefficient (Anode/Cathode)	$D_{ij,K} = \frac{2}{3}\, d_p \sqrt{\frac{2\,R\,T}{2\pi\left(\frac{1}{MW_i} + \frac{1}{MW_j}\right)^{-1}}}$	[24]
Bruggerman diffusion model (Gold paste)	$D_{ij}^{eff} = D_{ij} \cdot \frac{\varepsilon_{Au}}{\varepsilon_{Au}^{-0.5}}$	Built in COMSOL Multiphysics
Bosanquet effective binary diffusion (Anode/Cathode)	$D_{ij\,;\,A/C}^{eff} = \frac{\varepsilon_{A/C}}{\tau_{A/C}}\left(\frac{D_{ij} \cdot D_{ij,K}}{D_{ij} + D_{ij,K}}\right)$	[25]

#Fuller diffusion volume (v_i) data available in Appendix

MW_i= molecular weight of generic species *i* ; A=Anode ; C=Cathode; Au=gold paste

Secondary Current Distribution module

The electrochemistry and the transport of charge of the system, whether ionic and/or electric, is described through this module. This module applies to the MEA structure, i.e. the assembly of anode, cathode and electrolyte, plus the gold paste layers. The transport of charged species follows the Ohm's law and will be specifically described for each domain.

- *Gold paste interconnect*

The electric current transport in the porous gold interconnect is modeled through the conservation of electric charge equation:

$$\nabla\left(-\sigma_{e,Au}\,\nabla\phi_s\right) = 0 \tag{2.7}$$

where $\sigma_{e,Au}$ represents the bulk electronic conductivity of the metallic phase $[S/m]$ and ϕ_s is the electrostatic potential $[V]$. Since the equation is set equal to zero, no electrical current source is present. This is quite obvious because there are no active sites within the interconnect, and the only purpose of the gold paste is to connect the SOFC to the external load.

- *Porous electrodes*

The electronic charge transport within the porous electrodes is modeled through the equation:

$$\nabla\left(-\sigma_{e,A/C}^{eff}\,\nabla\phi_s\right) = \lambda_{TOT,A/C}^{TPB}\,S_{e,m} \tag{2.8}$$

where $\sigma_{e,A/C}^{eff}$ represents the effective electric conductivity at anode or cathode side, $\lambda_{TOT,A/C}^{TPB}$ represents the total TPB length per unit volume $[1/m^2]$ and S_e is the electronic charge source/sink term [A/m] due to the generic electrochemical reaction m. Both the effective conductivities and the total TPB per unit length will be evaluated and described in the next paragraph via Percolation theory. An additional equation is added in order to describe the ionic current transport:

$$\nabla\left(-\sigma_{io\,,A/C}^{eff}\,\nabla\phi_{el}\right) = \lambda_{TOT,A/C}^{TPB}\,S_{io,m} \tag{2.9}$$

where $\sigma_{io\,,A/C}^{eff}$ is the effective ionic conductivity, ϕ_{el} is the electrolyte potential and S_{el} is the ionic charge source/sink term [A/m]. Source/sink terms need to be coupled with the source/sink terms in the mass conservation equations. Indeed, in the anode porous layer hydrogen is consumed forming steam while, at the cathode side, oxygen is consumed. They can be expressed as:

$$S_{H_2} = -\frac{MW_{H_2}\,i_A}{2\,F} \tag{2.10}$$

$$S_{H_2O} = +\frac{MW_{H_2O}\, i_A}{2\, F} \tag{2.11}$$

$$S_{O_2} = -\frac{MW_{O_2}\, i_C}{4\, F} \tag{2.12}$$

where $i_{A/C}$ is the anodic/cathodic current density [A/m]. Furthermore, when evaluating the source/sink term in the charge conservation equations, the electronic current density is a sink term in the anode/cathode domain ($S_{e,m} = -i_{A/C}$), while the ionic current density is a source term in the anode/cathode domain ($S_{io,m} = +i_{A/C}$). Both the anodic and cathodic current densities can be evaluated by using a modified Butler-Volmer equation, that considers also the concentrations of the gaseous species in the active layers:

$$i_{A/C} = i^0_{A/C}\left[C_R \exp\left(\frac{\alpha^{anodic}_{A/C} F\, \eta}{RT}\right) - C_O \exp\left(\frac{-\alpha^{cathodic}_{A/C} F\, \eta}{RT}\right)\right] \tag{2.13}$$

where C_R and C_O are the normalized concentrations of oxidized and reduced species, i^0 is the exchange current density $[A/m]$, α is the electron transfer coefficient and η is the overpotential $[V]$. The voltage of the SOFC is evaluated based on the equilibrium voltages anode and cathode side as well as the polarization losses:

$$V_{cell} = V_{eq,C} - V_{eq,A} - \eta = OCV - \eta \tag{2.14}$$

The boundary conditions for the electrostatic potentials ϕ_s are applied at the top of the gold paste, which covers the cathode, and at the bottom of the gold paste, that covers the anode. Therefore, the potential difference between anode and cathode current collectors can be expressed as:

$$\phi_{s,AuC} = V_{cell} \tag{2.15}$$

$$\phi_{s,AuA} = 0 \tag{2.16}$$

This way, the potential at the anode current collector is used as a reference value.

- *Electrolyte*

Regarding the electrolyte only ionic conduction is considered since it is an electrical insulator. This means that only the transport of oxygen ions is considered.

No sink/source terms are needed since the electrolyte is a dense impermeable layer without the presence of PEAS. The charge conservation equation can be written as:

$$\nabla(-\sigma_{el}\nabla\phi_{el}) = 0 \tag{2.17}$$

2.4.4 Models based on Percolation Theory

In order to evaluate the effective properties such as ionic and electrical conductivities, TPB length per unit volume and the average electrode pore diameter, two different models based on Percolation Theory were used. Percolation Theory is purely based on a geometrical dissertation of the electrodes, starting from their microstructural features and manufacturing techniques. The estimate of the effective parameters depends on:

- Volumetric fraction of particles (ψ_i) that compose the electrode
- Mean diameter of the particles ($d_{p,i}$)
- Porosity (ε) and tortuosity (τ)
- Intrinsic conductivities of the materials involved (σ_i^0)

In Table 2.6 are summarized microstructural and intrinsic features for both anode and cathode.

Table 2.6. Parameters needed to apply Percolation theory

Parameters	***Value***	***Reference***
Cathode composed of LSCF and CGO particles		
$d_{p,LSCF}$	0.6 μm	[27]
$d_{p,CGO}$	0.6 μm	[27]
ψ_{LSCF}	0.53	This work
ψ_{CGO}	0.47	This work
τ_C	2	This work
$\sigma^0_{e,LSCF}$	$1.05 \cdot 10^4 [S/m]$	[28]
$\sigma^0_{io,LSCF}$	$0.4[S/m]$	[29]
$\sigma^0_{io,CGO}$	$5.9[S/m]$	This work[#]
Anode composed of Cu and CGO particles		
$d_{p,CGO}$	0.38 μm	[30]
$d_{p,Cu}$	0.3 nm	This work
ψ_{Cu}	0.35	This work

ψ_{CGO}	0.65	This work
τ_A	2	This work
$\sigma^0_{io,CGO}$	$5.9[S/m]$	This work[#]
σ^0_{Cu}	$10^7[S/m]$	This work

[#]Reasonable value that can be found in literature [46,38]

Subscripts: e=electronic conducting phase io=ionic conducting phase

The models used to derive the aforementioned effective parameters are treated separately, due to the differences in the electrode characteristics. First, a brief description of Percolation Theory and the parameters that characterize it is provided.

Percolation Theory

Percolation Theory studies from a statistical point of view the connections that occur in systems with multiple entities. In the specific case of an electrode, percolation theory evaluates how particles that compose it are distributed connecting each other and forming clusters. This theory is based on two key parameters: percolation probability and coordination number. Percolation probability represents the likelihood that particles are clustered in ways that form connected conduction pathways, ionic and electronic. Without creating clusters capable of conducting charged species, SOFCs would not be able to operate. On the other hand, the coordination number represents the number of contacts that a particle makes with its neighbouring particles. The coordination number for a generic *k* particle in a binary solid mixture (M=2; *k* and *l* particles) can be evaluated as [31]:

$$Z_{k,l} = 0.5\left(1+\frac{r_k^2}{r_l^2}\right)\bar{Z}\frac{\frac{\psi_l}{r_l}}{\sum_{k=1}^{M}\frac{\psi_k}{r_k}} \tag{2.18}$$

where r is the radius of the *k* or *l* particle, ψ is the solid volume fraction and $\bar{Z}$ is the average coordination number usually set equal to 6 [31]. Equation (2.18) is equally applicable for $k=l$ and $k \neq l$.

Before defining the percolation probability, it is worth to notice what type of clusters can be found in an electrode. For example, Figure 2.10 shows a binary packed mixture of spherical particles where three different clusters are represented for ion conductive particles.

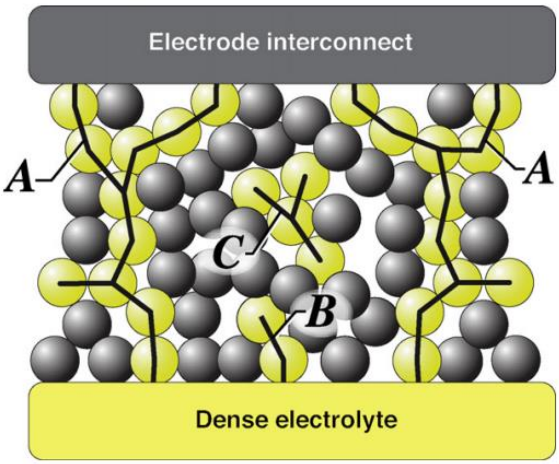

Figure 2.10. *Cluster in a composite SOFC electrode. Dark particles represent the electronic conductive phase while the yellow particles represent the ionic conducting phase.*

As observable there are three different clusters:

- *Clusters A:* here the percolated clusters cross the entire porous domain starting from the outer surface (electrode interconnect) down to the dense electrolyte.

- *Clusters B:* in this case a short chain of particles is formed which is in contact with the electrolyte surface. Although they can carry charged species, these clusters make a negligible contribution.

- *Clusters C:* these clusters are not connected with the electrolyte surface and therefore they are not able to provide ionic or electronic charge transfer.

The probability that particles belong to a *A* ionic/electronic cluster can be defined as [31]:

$$P^{e} = 1 - \left(\frac{4.236 - Z_{e,e}}{2.472}\right)^{3.7} \tag{2.19}$$

$$P^{io} = 1 - \left(\frac{4.236 - Z_{io.io}}{2.472}\right)^{3.7} \tag{2.20}$$

where $Z_{e,e}$ and $Z_{io,io}$ can be expressed by means of (2.18).

Cathode percolation theory-based model

The cathode is a composite electrode made by CGO, ionic conducting phase, and LSCF, a MIEC material capable of providing both ionic and electronic conduction. The peculiarity of this electrode is that both the solid phases can form ion conductive clusters. Therefore, it is immediate to state that the probability for the CGO and LSCF particles to form *A* clusters is unitary [33]:

$$P_{CGO}^{io} = P_{LSCF}^{io} = 1 \tag{2.21}$$

On the other hand, the electrical conductivity of the electrode is only attributable to the LSCF solid particles and the probability of forming *A* type clusters can be evaluated as:

$$P_{LSCF}^{e} = 1 - \left(\frac{4.236 - Z_{LSCF,LSCF}}{2.472}\right)^{3.7} \tag{2.22}$$

where $Z_{LSCF,LSCF}$ is evaluated via (2.18).
As regards the evaluation of the active sites, i.e. the TPB length per unit volume, two contributions (clearly distinguishable in Figure 2.11) were assessed:

1. TPB due to the presence of three different phases, i.e. gas phase, LSCF and CGO solid phases. In this case, the active sites are located along the 1-D circular length between LSCF and CGO particles.

2. DPB due to the presence of pure MIEC material. In this case, the active sites are located on the entire free surface of the LSCF particles in direct contact with the gas phase. Since MIEC are mixed conductor, the presence of a third phase (ionic or electronic) is not necessary for the reactions to take place.

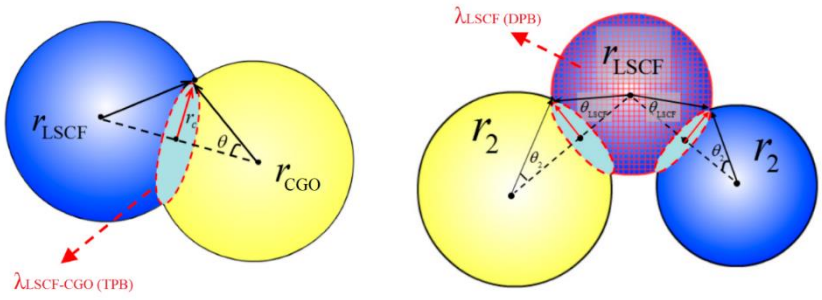

(a) *(b)*

Figure 2.11.*(a) Sketch of electrochemical reaction site per contact between LSCF and CGO particles (b) exposed free surface area of LSCF particles able to promote reactions [Adapted from 32].*

The effective percolated TPB length per unit volume is evaluated as function of the electrode composition and microstructural characteristics:

$$\lambda_{LSCF-CGO}^{eff} = \gamma_{LSCF-CGO}\, n_{LSCF}^{V}\, Z_{LSCF-CGO}\, P_{LSCF}^{e}\ [1/m^2] \tag{2.23}$$

Where:

- $\gamma_{LSCF-CGO} = 2\pi \cdot \min(r_{LSCF}, r_{CGO}) \sin\theta$, represents the circumference at the interface between two sintered particles. The contact angle θ depends on the contact radius r_c and it is initially assumed to be 15° [31,32,33], and then used as a fitting parameter for the optimization.

- $n_{LSCF}^{V} = [(1-\varepsilon_C)\psi_{LSCF}]/[4/3\,\pi r_{LSCF}^3]$, represents the number of LSCF particles per unit volume.

- $Z_{LSCF-CGO}$, represents the mean number of contacts between LSCF particles and all of its neighbouring CGO particles. It is evaluated using equation (2.18).

- P_{LSCF}^{e} is the percolation probability evaluated as in equation (2.22).

The effective percolated DPB per unit volume is a function of the number of LSCF particles per unit volume, the free surface exposed to the gas phase and the percolation probability of LSCF particles forming *A* type conductive clusters. It can be evaluated as:

$$\lambda_{DPB}^{eff} = n_{LSCF}^{V}\, s\, P_{LSCF}^{e} P_{LSCF}^{io}\ [1/m] \tag{2.24}$$

where *s* is the free surface, calculated by subtracting from the total surface of a LSCF particle the contact surface of the particles to which it is bound. It is evaluated as:

$$s = 2\pi r_{LSCF}^2 \left(2 - (1-\cos\theta_{LSCF}) Z_{LSCF,LSCF} - (1-\cos\theta_{LSCF}) Z_{LSCF,CGO}\right) \tag{2.25}$$

where the contact angle θ_{LSCF} is initially assumed to be equal to 15° [31,32,33]. Since the contact angle depends on the particles size involved and, in this thesis, both LSCF and CGO have same particle size, θ_{LSCF} is assumed to be equal to θ. While this is a reasonable assumption for the cathode, it is not possible to use a single contact angle at the anode given the difference in particles size. The effect of uncertainty in the contact angles is evaluated in Chapter 4 by sensitivity analysis. It is worth to notice that, the percolated TPB has the unit of $1/m^2$ while the percolated DPB has the unit of $1/m$. In order to obtain a single global

value for the TPB cathode side ($\lambda_{C,TPB}^{TOT}$), the value of $\lambda_{DPB}^{eff}$was scaled multiplying by the ratio between the total exposed surface of the MIEC and the total volume of the electrode. The total exposed LSCF surface area can be evaluated starting from the exposed surface of a single LSCF particle *s*, calculated using equation (2.25), multiplied by the number of LSCF particles. This value is then divided by the volume of the electrode whose geometry is known.

To evaluate the effective conductivities, the fact that interfaces between particles might have different properties than the particle body is taken into account. Thus, the effective electronic or ionic conductivity through the composite cathode can be separated into intra-particle conductivity and inter-particle conductivity [31,32,33]:

$$\sigma_{k/l\,,e/io}^{tra,eff} = \sigma_{k/l,\,e/io}^{0}\ \left(\psi_{k/l}\,(1-\varepsilon_C)\right)^{\mu}\ \left[\frac{S}{m}\right] \tag{2.26}$$

$$\sigma_{k-l,e/io}^{ter,eff} = \frac{\sigma_{kl,e/io}^{ter,0}\left(4\ a_{kl}\ \min(r_k,r_l)^2\ n_k^V\ Z_{k,l}\ P_k^{io} P_l^{io}\right)}{\delta}\ \left[\frac{S}{m}\right] \tag{2.27}$$

where $\sigma_{k/l,\,e/io}^{0}[S/m]$ is the bulk conductivity (ionic or electronic) for the generic species *k* or *l*, $\sigma_{k-l,e/io}^{ter,0}[S/m]$ is the inter-particle bulk conductivity (ionic or electronic) between *k* and *l* particles, $\sigma_{k/l\,,e/io}^{tra,eff}\ [S/m]$ is the intra-particle effective conductivity, $\sigma_{k-l,e/io}^{ter,eff}\ [S/m]$ is the inter-particle effective conductivity, μ is the Bruggeman factor and $\delta[m]$ is the thickness of the interface between the particles in contact. Notice that δ is often assumed to be 5 nm [33,34], the Bruggeman factor is usually set equal to 1.5, and $\sigma_{kl,e/io}^{ter,0}$ is assumed to be two order of magnitude smaller than the bulk intra-particle conductivity [34]. As for electronic conductivity, this is limited by the restriction between particles in contact. This means that the intra-particle resistance is negligible compared to the inter-particle resistance. Therefore, the net effective electrical conductivity of the electrode is evaluated only considering equation (2.26). On the contrary, the ion conductivity is limited by both inter/intra particle resistance equally. The net effective ionic conductivity is then calculated as the inverse of the sum of resistances in parallel [33,34]:

$$\sigma_{C,io}^{net,eff} = \left(\frac{1}{\sigma_{CGO,io}^{tra,eff} + \sigma_{LSCF,io}^{tra,eff}} + \frac{1}{\sigma_{LSCF-LSCF,io}^{ter,eff} + \sigma_{CGO-CGO,io}^{ter,eff} + \sigma_{LSCF-CGO,io}^{ter,eff}}\right)^{-1} \tag{2.28}$$

Finally, this model also allows to estimate the average pore radius starting from the microstructural features of the electrode. It can be evaluated as:

$$r_{p,C} = \frac{2}{3}\left(\frac{\varepsilon_C}{1-\varepsilon_C}\right)\left(\frac{\psi_{LSCF}}{r_{LSCF}} + \frac{\psi_{CGO}}{r_{CGO}}\right)^{-1} \tag{2.29}$$

In Table 2.7 the calculated effective properties are listed.

Table 2.7. Output data from Cathode percolation theory model

Parameter	*Value*
$\lambda_{C,TPB}^{TOT}$	$7.19 \cdot 10^{13}[1/m^2]$
$\sigma_{C,io}^{net,eff}$	$0.62[S/m]$
$\sigma_{C,e}^{net,eff}$	$1887.6[S/m]$
$r_{p,C}$	$5 \cdot 10^{-8}[m]$
$D_{p,C}$	$6 \cdot 10^{-7}[m]$
K_C	$3 \cdot 10^{-17}[m^2]$

Anode percolation theory-based model

Effective properties for the anode cannot be evaluated using the model described above. This is due to the difference in the microstructural characteristic between the two electrodes. While the cathode is composed by particles having similar diameters, in the anode - manufactured via impregnation method - Cu particles are about ten times smaller than CGO particles. A schematic illustration of a nanoparticle impregnated electrode can be seen in Figure 2.12. Therefore, a specific model for impregnated electrodes will be used in order to derive effective properties. However, currently the description of impregnated electrodes is more difficult than that of the well-known composite electrodes, which means that few models are present in literature.

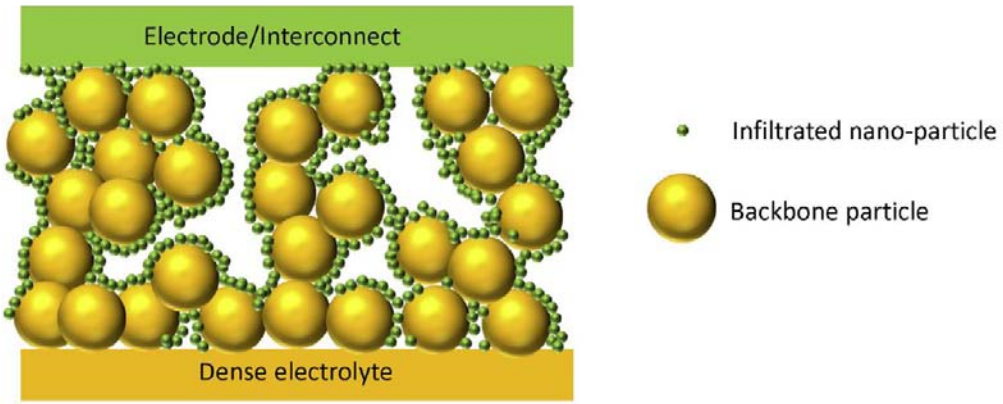

Figure 2.12. *Scheme of an impregnated electrode where the ion conducting particles form the porous framework (Backbone) covered by electronic conducting nanoparticles [35].*

The model used in this thesis is based on two assumptions:

1. The electrode framework consists of a random packing of spherical CGO particles.

2. The framework is covered by a coating of spherical nanometric Cu particles.

In order to simplify the understanding of the formulas characterizing this model, it is necessary to depict the geometrical details as in Figure 2.13.

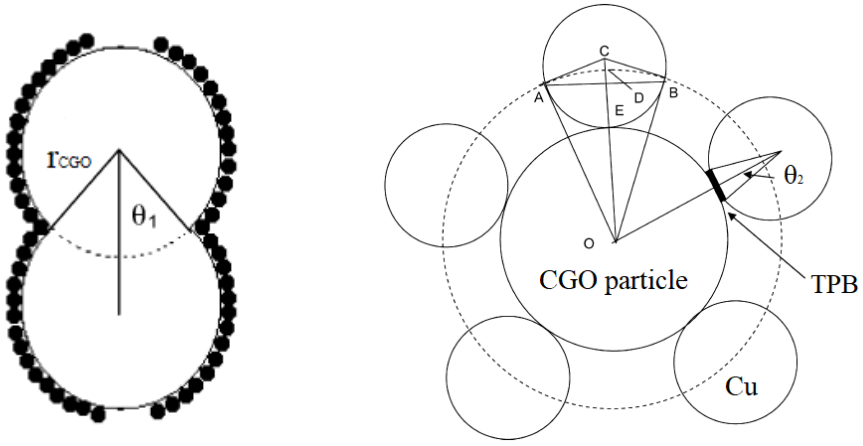

Figure 2.13. *a) Single phase contact between CGO particles b) Two phase contact between CGO and Cu particles with the magnification of the TPB [Adapted from 36].*

The CGO particles, when sintered together, lose a portion of the surface which cannot be covered by Cu nanoparticles. This surface can be evaluated as:

$$A_d = 2\pi r_{CGO}^2(1 - \cos\theta_1) \tag{2.30}$$

where θ_1 is the contact angle between CGO particles initially assumed to be 15° and then used as a fitting parameter. The number of CGO particles per unit volume composing the electrode backbone is calculated as:

$$n_{CGO}^V = (1 - \varepsilon_f)/\left(\frac{4}{3}\pi r_{CGO}^3\right) \tag{2.31}$$

where ε_f is the framework porosity assumed to be equal to 0.41 [36]. This value can vary from 0.25 up to 0.55 depending on the volume fraction of the pore former used as well as other processing details [37]. For that reason, the effect of changes in ε_f value is then studied

in Chapter 4. At this point it is possible to evaluate the free CGO particles surface per unit volume, i.e. the surface that can be covered by Cu nanoparticles, through the relation:

$$A_E = -\frac{3}{2r_{CGO}}\left(20.7(1-\cos\theta_1)\varepsilon_f^2 - (35.05 - 37.05\cos\theta_1)\varepsilon_f - 16.35\cos\theta_1 + 14.35\right) \tag{2.32}$$

The analytical derivation of this equation is quite complex and involves Percolation theory; more details in reference [36]. At this point, it is necessary to evaluate the maximum number of Cu particles capable of completely covering the free surface of the electrode backbone. In order to do that, an imaginary sphere with radius *OD* (represented in Figure 2.13 b)) is considered. The area of this hypothetical sphere occupied by Cu nanoparticles is:

$$A_c = 2\pi\left[-\frac{\left(r_{CGO}(r_{CGO}+2r_{Cu})\right)^{3/2}}{r_{CGO}+r_{Cu}} + r_{CGO}(r_{CGO}+2r_{Cu})\right] \tag{2.33}$$

where $r_{CGO} = OE$ and $r_{Cu} = CE$ in Figure 2.13. The maximum number of nanoparticles capable of occupying the free surface of the electrode backbone is given by:

$$N_{Cu}^0 = (4\pi(r_{CGO}+r_{Cu})^2 \cdot 0.907)/A_c \tag{2.34}$$

where 0.907 is the "maximum packing factor" in a 2-D packed sphere system [36].
Considering that not all the available surface could be covered by the coating, the number of Cu nanoparticles per unit volume is defined as:

$$n_{Cu}^V = \lambda\, N_{Cu}^0 \frac{A_E}{4\pi r_{CGO}^2} \tag{2.35}$$

where λ represents the coverage fraction and it is typically bounded between 0 and 1. Notice that, in impregnated electrodes, its value must be greater than a certain critical value λ_{crit} in order to produce a coating capable of conducting electric charge. The coverage fraction values assumed in this thesis is 0.9, often used in literature, while the critical coverage value is set equal to 0.5 [37]. When $\lambda \geq \lambda_{crit}$ it is possible to evaluate the TPB length per unit volume as:

$$\lambda_{A,TPB}^{TOT} = 2\pi r_{Cu}\sin\theta_2\, n_{Cu}^V \tag{2.36}$$

where θ_2 is the contact angle between CGO and Cu particles initially assumed to be 15° and used, also in this case, as a fitting parameter.

As regards the estimate of the actual conductivities for the anode, these have been evaluated according to two different methods. For the ionic effective conductivity, the same dissertation seen for the cathode is used considering that only CGO particles provide for ion exchange. Therefore, the net effective ionic conductivity is given by the combination of (2.26) and (2.27):

$$\sigma_{A,io}^{net,eff} = \left(\frac{1}{\sigma_{CGO,io}^{tra,eff}} + \frac{1}{\sigma_{CGO-CGO,io}^{ter,eff}} \right)^{-1} \tag{2.37}$$

On the other hand, the evaluation of the electronic conductivity considers the formation of a more or less homogeneous layer of Cu on the CGO backbone. Since no percolated Cu particles are present in an impregnated electrode, the net effective electronic conductivity of the anode is evaluated starting from the bulk conductivity of the material multiplied by three parameters (f_i), whose values are less than one [37]. Therefore, the net effective electronic conductivity is calculated as:

$$\sigma_{A,e}^{net,eff} = \sigma_{Cu,e}^{0} \cdot \prod_{i=1}^{3} f_i = \sigma_{Cu,e}^{0} \left(\frac{\lambda - \lambda_{crit}}{1 - \lambda_{crit}} \right)^{1.3} \cdot \left(\frac{R_{film}}{R_{eff}} \right) \cdot \left(\frac{\psi_{Cu}}{\tau_s} \right) \tag{2.38}$$

where the first contribution f_1 takes into account the inhomogeneity of the coating upon the CGO particles, the second contribution f_2 considers the difference between the resistance to the charge flow offered by an ideal continuous coating layer and a pseudo-continuous coating layer (as in reality) and finally, the third contribution is given by the ratio between the Cu volumetric fraction and the tortuosity of the coating itself. The evaluation of (2.38) is based on literature values reported in Appendix.

As seen for the cathode, the model ends with the estimate of the average pore radius. The relation used is the same as (2.29) but, in this case, it has been assumed that the electrode is composed of "super-particles" with radius $r_{sp} = r_{CGO} + r_{Cu}$. Although this assumption may seem very simplifying, it is reasonable to think that as the conventional composite electrodes are well described by a random packing sphere model, this nanoparticle infiltrated electrode may be described by a random packing of "super-particles". The super-particle consists of a backbone particle plus a shell of infiltrated nanoparticles on its surface.

To conclude, the mean anode pore radius can be evaluated as:

$$r_{p,A} = \frac{2}{3} \left(\frac{\varepsilon_A}{1 - \varepsilon_A} \right) \left(\frac{1}{r_{sp}} \right)^{-1} \tag{2.39}$$

In Table 2.8 the calculated effective properties are listed.

Table 2.8. Output data from Cathode percolation theory model

Parameter	***Value***
$\lambda_{A,TPB}^{TOT}$	$4.39 \cdot 10^{14}[1/m^2]$
$\sigma_{A,io}^{net,eff}$	$1.007[S/m]$
$\sigma_{A.e}^{net,eff}$	$5.37 \cdot 10^{5}[S/m]$
$r_{p,A}$	$5.85 \cdot 10^{-8}[m]$
$D_{p,A}$	$4.1 \cdot 10^{-7}[m]$
K_A	$6.17 \cdot 10^{-17}[m^2]$

Chapter 3

Model Validation and results

In this chapter, the validation of the model by fitting the experimental data is reported. The fitting was carried out using the Optimization module available in COMSOL Multiphysics. As explained in Chapter 1 (see reference 1.3.2, 1.3.3), it is possible to characterize a cell via Electrochemical Impedance Spectroscopy (EIS) and via Polarization Curve (PC). Since the EIS is the most sensitive among the two methods, it was first used to regress kinetic and microstructural parameters, such as the exchange current densities and the contact angles between sintered particles. Once the optimal parameters were obtained, the cell was also compared to PC measurements.

3.1 EIS Curve Optimization

SOFCs are complex system governed by several coupled processes where electrochemistry, charge transport and mass transport simultaneously occur. Because polarization curves can only provide a general description of the cell performance, EIS has become a widely used characterization method. Moreover, it involves relatively simple electrical measurement thanks to which it is possible to find detailed information about the fuel cell system, ranging from the mass transport up to the charge transport phenomena [39]. As seen in 1.3.3, this characterization is based on the measure of the impedance by forcing the cell with a small input perturbation (usually in the voltage), and changing the frequencies, usually from 0.01 Hz up to 10^6 Hz, resulting in the construction of the impedance spectra. The final result - that is the impedance measured - is then plotted in the Nyquist plot. However, its application often encounters measurement issues because of the presence of parasitic inductances due to the electromagnetic interaction between connected cables, external instruments and the gold paste interconnect. Although parasitic inductances influence the whole impedance spectra, their effect is strongly marked at high frequencies [39]. Errors caused by parasitic inductances can limit the measurement quality, lead to inaccurate parameters identification and deform the EIS curve [40]. Since the modeling of these phenomena goes beyond the purpose of this thesis, the fitting and validation of the EIS curve is done following this methodology:

1. Initially, under the advice of researchers form the Chemistry Department of Padua, the experimental EIS curve is optimized by neglecting experimental impedance points at frequency greater than $5 \cdot 10^5\ Hz$. It should be noted that the experimental curve, shown in Figure 3.1, is obtained at OCV condition by varying the frequency spectrum from $0.01\ Hz$ up to $10^6\ Hz$, and at a temperature of 650°C.
   Notice that points in the negative part of the Nyquist plot are due to the presence of the parasitic inductances, and they do not describe any physical or chemical phenomena occurring within the SOFC studied. The area marked in red represents the area most subjected to the parasitic inductance influence. The inability to properly fitting the curve, especially the impedance points below zero without any physical meaning attributable to the cell, has been solved as described above.

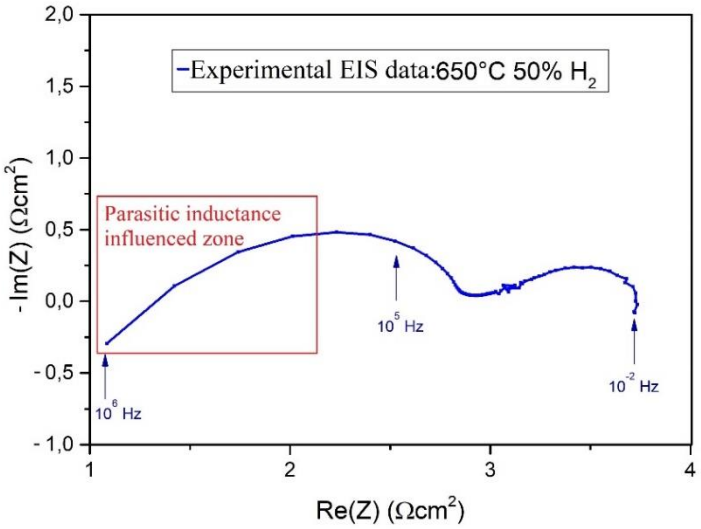

Figure 3.1. *Experimental EIS curve evaluated at 650°C. Red box defines the EIS parasitic inductance influenced area.*

2. Once the optimization of the EIS curve has been conducted, in order to completely close the high frequency arc, the frequency spectrum analysed was arbitrarily increased up to $10^8\ Hz$. This is only a "mathematical trick" used to close the left arc of the Nyquist plot. In fact, the impedance values obtained beyond the optimized range cannot be compared with the real ones. Therefore, this is a way to obtain a graphic similarity between experimental and calculated curves, disregarding the effect of parasitic inductances.

The detailed description of these two points and their results are now reported.

3.1.1 EIS Optimization disregarding parasitic inductance effect

The Optimization module is used to fit experimental data. The procedure is divided into three steps. Firstly, the objective function needs to be defined. Secondly, both different project variables - that is, the values to be modified - and constraints - that is, the ranges in which the chosen variables can vary - are defined. Finally, the Optimization module is used to improve the simulation results by modifying the chosen variables, satisfying the imposed constraints, in order to minimize the objective function. The general formulation of an optimization problem can be written as [41]:

$$\begin{cases} \min_{\zeta} Q(\zeta) \\ \zeta \in C \end{cases} \tag{3.1}$$

where ζ represents the vector of the control variables, Q represents the scalar objective function and C represents the constraints. It can be expressed as:

$$C = [\zeta : lb \leq G(\zeta) \leq ub] \tag{3.2}$$

where G is a vector-valued function, lb and ub are the vectors containing the upper and lower bounds of the constraints respectively. The initial values of the project variables are shown in Table 3.1.

Table 3.1. Project variables values before optimization

Parameter	*Value*	*Constraints*	*Ref*
Cda	0.1 $[F/m^2]$	$0.001 \leftrightarrow 10$	[42,43]
Cdc	1 $[F/m^2]$	$0.001 \leftrightarrow 10$	[42,43]
i_A^0	10^{-7} $[A/m]$	$10^{-9} \leftrightarrow 10^{-4}$	This work
i_C^0	10^{-7} $[A/m]$	$10^{-9} \leftrightarrow 10^{-4}$	This work
α_A^{anodic}	0.3	$0.1 \leftrightarrow 1$	[2]
$\alpha_A^{cathodic}$	1.5	$0.1 \leftrightarrow 1$	[2]
α_C^{anodic}	0.7	$0.5 \leftrightarrow 2$	[2]
$\alpha_C^{cathodic}$	0.5	$0.1 \leftrightarrow 1$	[2]
θ_1	15°	$13° \leftrightarrow 30°$	This work
θ_2	15°	$13° \leftrightarrow 30°$	This work
θ	15°	$13° \leftrightarrow 30°$	This work

In the table, two parameters not yet discussed are shown: Cda and Cdc. These parameters represent the effect of the Double Layer Capacitance at anode and cathode side, respectively. In a SOFC the two electrodes are separated by the electrolyte, and two boundary layers are formed, i.e. anode-electrolyte layer and electrolyte-cathode layer. These layers can be charged by polarization effect, known as electrochemical double layer charging effect, during normal fuel cell operation. The layers can store energy and behave like a super-capacitor. The effect of double layer capacitance can be evaluated by the COMSOL model. However, their specific values are not easy to obtain, especially since they depend on many factors including electrode potential, temperature, species concentration, contact area between layers, etc [2]. Figure 3.2 shows the comparison of experimental and calculated data before the optimization process.

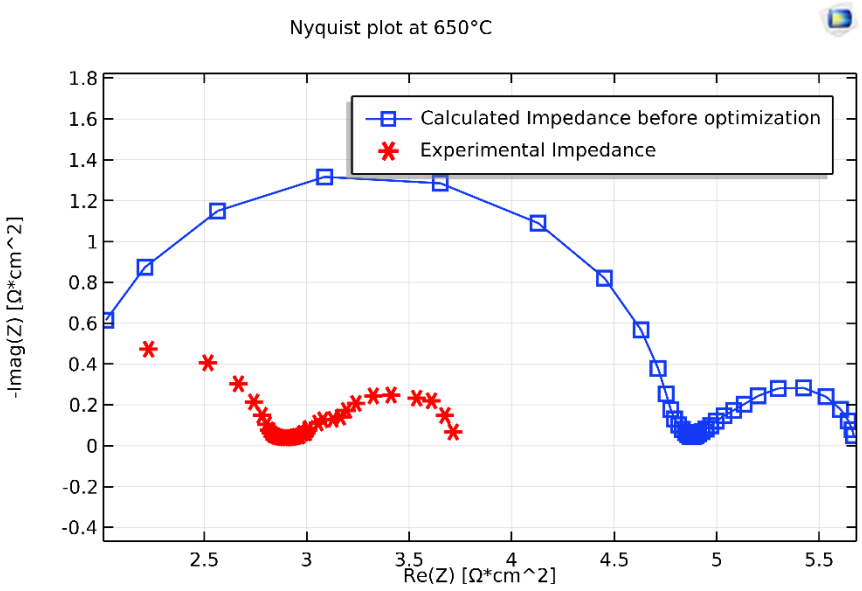

Figure 3.2. *Experimental and calculated EIS curves before the optimization process*

In the figure it is clearly visible that the high frequency impedance points - those that characterize the left arc - which typically describe electrochemical phenomena, are totally out of range. Instead, the low/medium frequency impedance points, characteristic of transport phenomena inside the cell, form an arc similar in size but shifted along the Re(Z) axis. That is because an optimization, mainly of kinetic parameters, needs to be performed. After several optimization processes needed to restrict the initial constraints range, the final result is the one shown in Figure 3.3. In order to make the optimized Nyquist plot easier to interpret - ensuring that impedance points have similar values at the same frequencies - the individual values of Re(Z) and -Im(Z) as a function of the analysed frequency spectrum have been plotted as well. These graphs are called Bode diagrams. As shown in the graph, the

model can offer a really good representation of the real cell studied. Particularly, at medium and high frequencies, the model returns results very consistent with the experimental one. As for the low frequency range, which are typically influenced by microstructural features of the cell and transport phenomena involved, the model provides just a fair representation of the real cell. Probably, this is caused by the not perfect modeling of the porous electrodes and by the uncertainty in some microstructural parameters, especially the porosities. This is particularly true for the anode, which is and impregnated electrode, because it is much more difficult to model with respect to a common composite electrode.

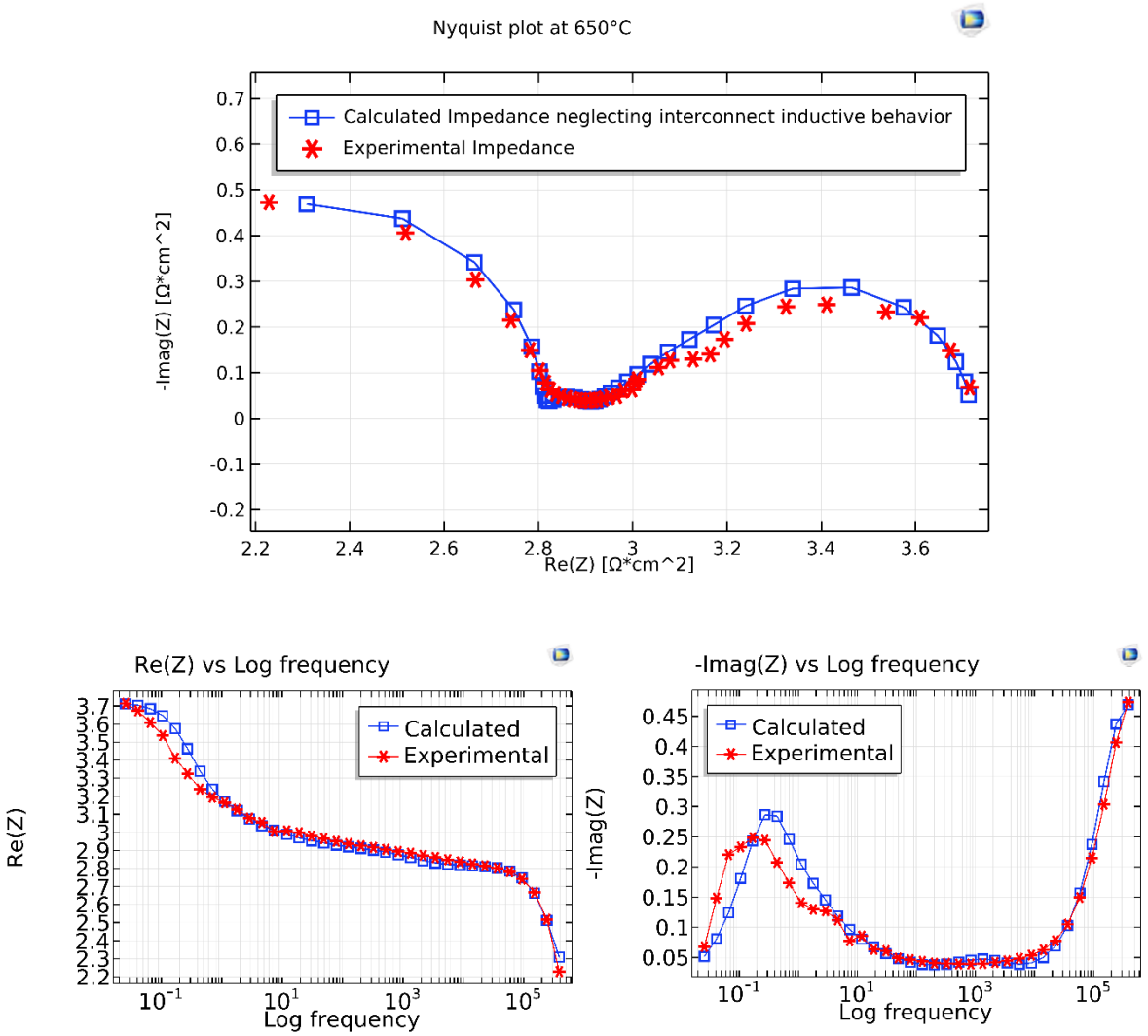

Figure 3.3. *Experimental and calculated EIS curves after the optimization process. On the top the optimized Nyquist plot, on the bottom the optimized Re(Z) and -Im(Z) vs the frequency (Bode plot).*

It is worth noticing that, for complex models such as SOFCs, a perfect agreement between experimental and calculated data is very difficult to obtain. The reasons can be several: approximations used in the model, presence of noise in the experimental data or physical

deterioration of the cell due to mechanical or thermal stress. The values of the optimized project parameters after the optimization are reported in Table 3.2.

Table 3.2. Project variables values after optimization

Parameter	*Value*
Cda	0.027 $[F/m^2]$
Cdc	0.69 $[F/m^2]$
i_A^0	4.71· 10^{-7} [A/m]
i_C^0	2.26· 10^{-7} [A/m]
α_A^{anodic}	0.3
$\alpha_A^{cathodic}$	1.6
α_C^{anodic}	0.7
$\alpha_C^{cathodic}$	0.33
θ_1	17.98°
θ_2	27.3°
θ	18.45°

From the results in the table, it is possible to see that none of these reach its upper or lower limit. This implies that the structure of the model is good, and it does not require huge variations in its fitting parameters to return good results. At this point, in order to close the characteristic arc of the high frequencies, the optimized model has been used to evaluate the EIS curve in a wide frequency range, up to $10^8 Hz$. As already mentioned, this is just a "mathematical trick" used to compare both experimental and calculated EIS curve, disregarding the effect of parasitic inductances. The result of this operation is represented in Figure 3.4, where Figure 3.4 a) represents the experimental curve and Figure 3.4 b) the calculated one.

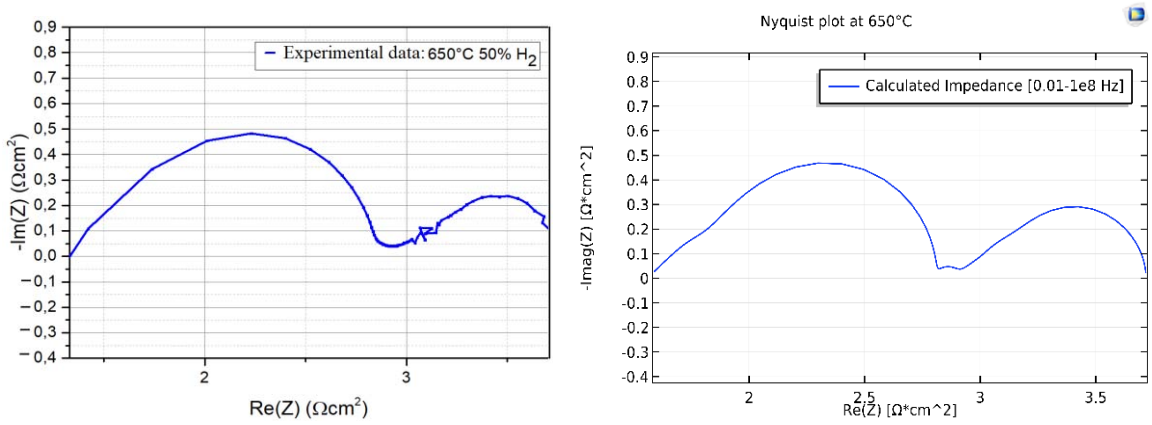

(a) *(b)*

Figure 3.4. *Comparison between calculated and experimental EIS curve.*

A good agreement exists between the two curves; therefore, it is possible to state that the model can simulate the operation of the cell. Notice that the final part of the left high frequency arc does not follow the same trend. That is because the calculated impedance values are not influenced by the parasitic inductances. Therefore, it loses its rounded shape.

3.2 Validation via Polarization curve

The validation of the model is completed with the polarization curves comparison. Also in this case, the validation requires a further optimization process. Since the experimental data relating to the polarization curve were obtained at 660°C, ten degrees more than the EIS, it was decided to use the optimized data obtained from the EIS optimization, varying only the parameters strongly influenced by the temperature. These parameters are the anodic/cathodic exchange current densities and the ionic conductivity of the CGO. Furthermore, since the permeability of the gold paste is unknown, this parameter was also used as a fitting parameter. All the other parameters have remained unchanged. It is worth to notice that, since the EIS Study on COMSOL does not solve the Brinkman equation, the effect of the gold paste permeability cannot be evaluated via EIS optimization. While the value of the gold permeability has been varied in a wide range, as far as the other parameters optimized are concerned (the exchange current densities) they have been varied in a very narrow range: up to 25% of their initial value. Although the difference of 10°C may seem negligible, both the exchange current densities and the ionic conductivity can be described using an Arrhenius law:

$$i^0_{A/C} = A \cdot f(p_i)^n \cdot \exp\left(-\frac{E_a}{RT}\right) \tag{3.3}$$

$$\sigma_{io,j} = A \cdot \exp\left(-\frac{C_j}{T}\right) \tag{3.4}$$

where A is the pre-exponential factor, $f(p_i)$ is a function of the reacting species partial pressure raised to an empirical exponent n, E_a is the activation energy and C_j is a characteristic constant for each ionic conductor. In Table 3.3 the values of the project variables before optimization are listed.

Table 3.3. Project variables values before optimization

Parameter	*Value*	*Constraints*
i^0_A	$4.71 \cdot 10^{-7}$ [A/m]	$4.71 \cdot 10^{-7} \leftrightarrow 5.89 \cdot 10^{-7}$
i^0_C	$2.26 \cdot 10^{-7}$ [A/m]	$2.26 \cdot 10^{-7} \leftrightarrow 2.83 \cdot 10^{-7}$
K_{Au}	10^{-16} $[m^2]$	$10^{-17} \leftrightarrow 10^{-14}$

The polarization curve, calculated with the initial estimate values, is represented in Figure 3.5. As shown, there is a growing difference between experimental and calculated data when the cell polarization increases. This effect is essentially caused by the temperature effect on the variables that will be optimized. As discussed in the last chapter, the effect of a small change in the exchange current densities causes a net change in the cell performance.

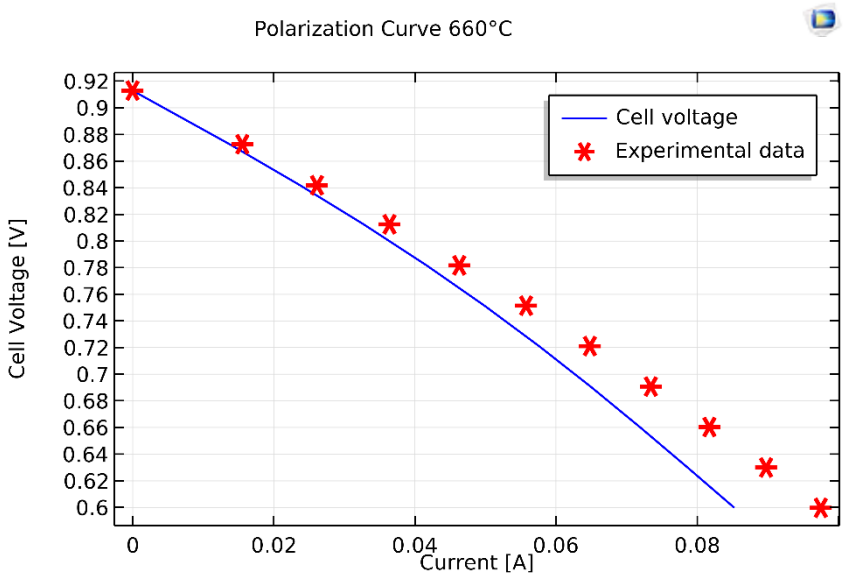

Figure 3.5. *Calculated PC vs experimental data before the optimization process*

After the optimization process, computationally lighter than that performed in the EIS optimization, the result in Figure 3.6 is found.

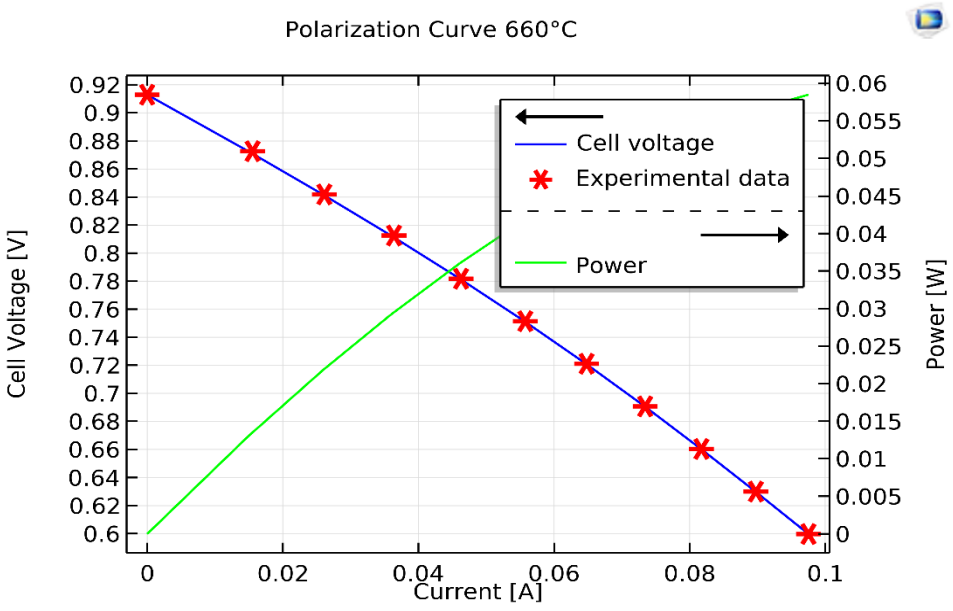

Figure 3.6. *Calculated PC vs experimental data after the optimization process*

The calculated curve can perfectly fit the experimental points, mainly because it is much less sensitive than the EIS characterization. For the sake of completeness, the power generated by the cell, given by the product between voltage and current, has been plotted as well. The values of the optimized project variables are listed in Table 3.4.

Table 3.4. Project variables values after optimization

Parameter	*Value*
i_A^0	4.92E-7 [A/m]
i_C^0	2.78E-7 [A/m]
K_{Au}	$1.72E-15$ $[m^2]$

3.3 Concentration Gradients and Fluid Dynamics

Once the model has been validated, it is possible to get information concerning the fluid dynamics of the system and the variation of the species within each domain. It is important to underline that these results cannot be easily obtained experimentally. Therefore, the aid of modeling is fundamental to obtain unknown data and, as it will be discussed in the last chapter, to improve operating conditions or key design parameters.

3.3.1 Calculated Fluid Dynamics

When discussing the Free and Porous Media Flow module (see paragraph 2.4.3), it was said that the velocity field of the gases is laminar. Additionally, a maximum inlet speed was also provided depending on inlet flowrate and geometry. These conclusions were drawn by means of the simulation, where it is possible to define the velocity field for each domain. Particularly, it becomes clear that gases move under convection inside the gas channel while, within the porous domain, diffusion predominates. Figure 3.7 shows the velocity field on the cathode side. Two different views have been reported. On the left, the 3-D representation of the cathodic compartment showing the gas phase motion. The maximum velocity is reached in the outlet gas section, caused by the external tube section restriction. The incoming gases brush the surface of the MEA structure and penetrate into the gold paste interconnect and electrode by diffusion, through a concentration gradient. In fact, in the porous domains the velocity is close to zero. Note that the areas in direct contact with the external/internal walls of the double hollow tube are characterized by a null velocity. This is due to the “no-slip velocity” boundary condition imposed at the walls. On the right, a more intuitive 2-D

representation of the motion of the fluid in the same compartment. The streamlines represent both the path and the velocity magnitude of the gas phase, according to the thickness of the arrows.

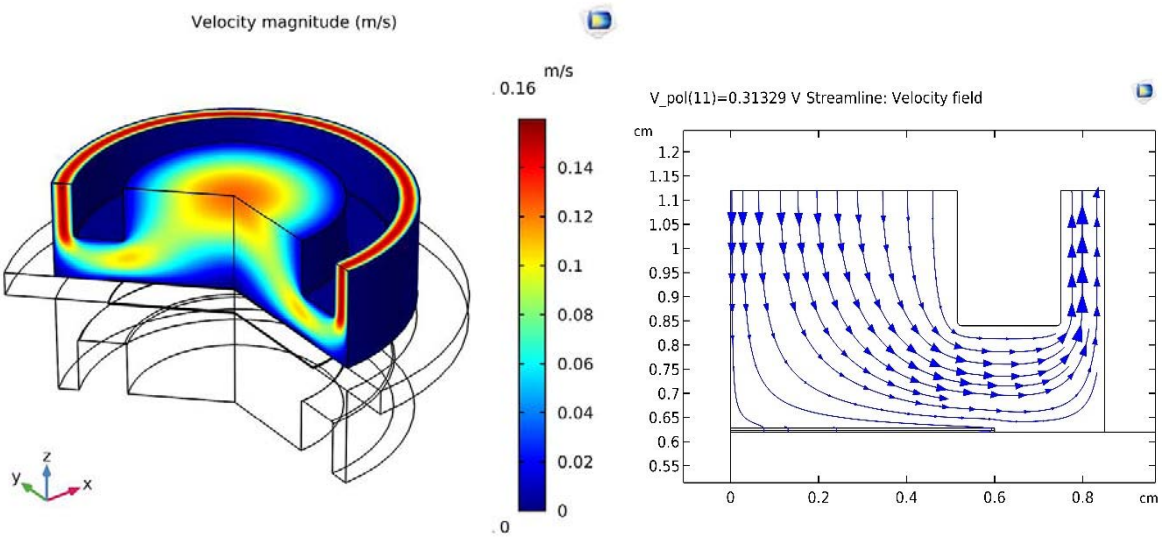

(a) *(b)*

Figure 3.7. *Fluid dynamics of the system with different views. (a) 3-D representation of the cathodic compartment; (b) 2-D representation using streamlines (same compartment as (a)).*

3.3.2 Molar fraction gradients

Through the simulation, it is also possible to evaluate how the species involved vary, that is react, within the various domains. The change in the molar fractions of hydrogen and oxygen has been evaluated. Particularly, oxygen will be consumed at the cathode while hydrogen will be consumed at the anode. It is expected that the larger gradients are concentrated where there is the presence of PEASs, which means inside the electrodes. In Figure 3.8 these gradients are represented by using two different views. Figure 3.8 a) and b) represent the overall cell view; here it is clearly visible how, in the gas channels, the variation of molar fractions is relatively low and tends to increase as it approaches the porous domains. This is due to the simultaneous occurrence of steps 1 and 4, described in Figure 1.1 (Paragraph 1.2.1). Instead, figure 3.8 c) and d) show changes in molar fraction within porous domains, in which the largest gradients occur. The larger peak of consumption can be found at the electrode/electrolyte interface. Notice that, inside the electrolyte domain, no gradients can be found. In fact, the electrolyte is modeled as a dense and non-permeable layer.

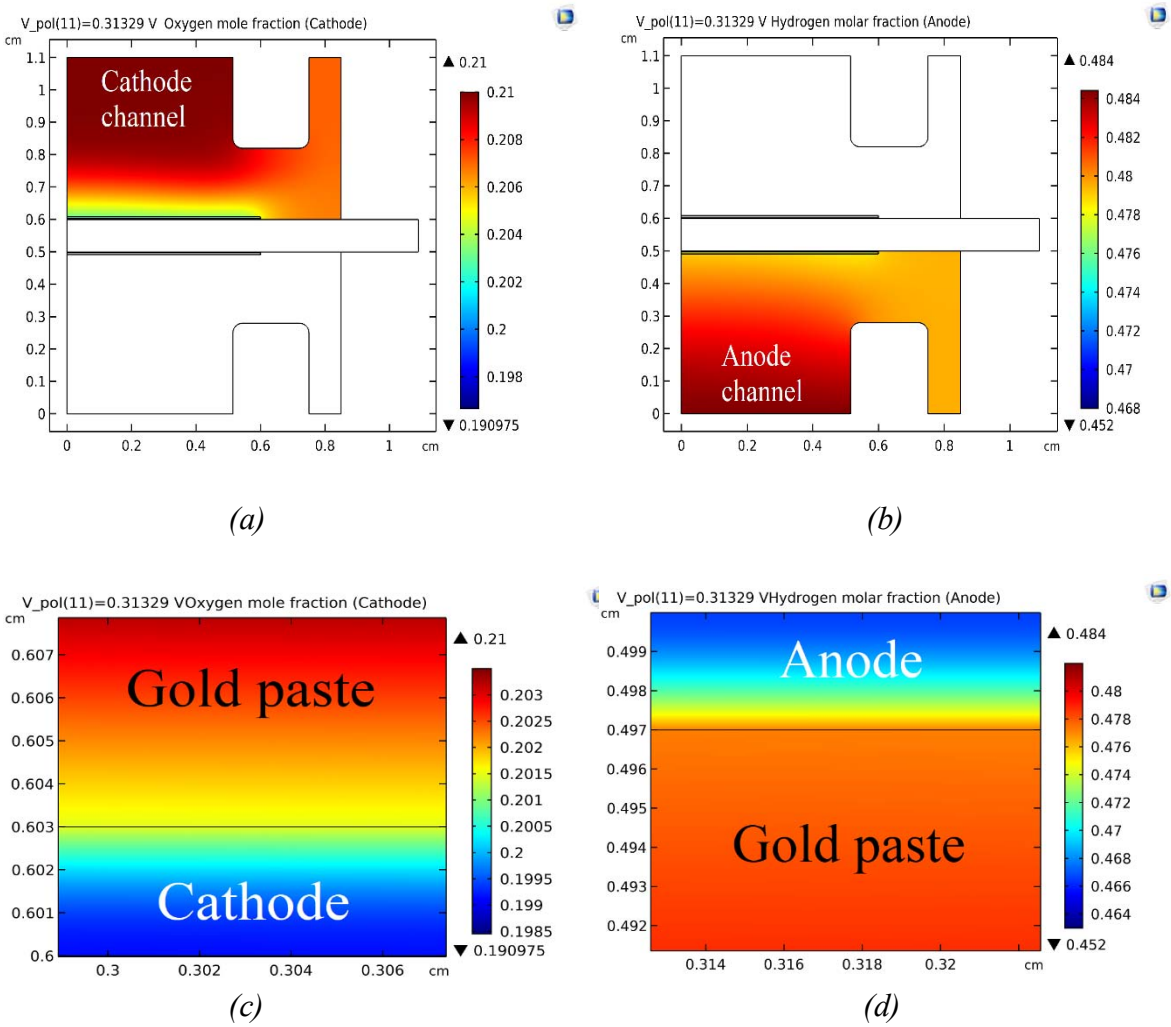

Figure 3.8. *Changes in molar fraction of hydrogen and oxygen. Figure (a,b) represent the global cell view while Figure (c,d) highlight gradients within the porous domains.*

As expected, this SOFC is not characterized by high performance and this results in a relatively low consumption of the reactant species coupled with low current delivered. Furthermore, the restricted range in concentration variation suggests that the cell operates under electrochemical limiting regime.

Chapter 4

Sensitivity Analysis

In this last chapter, the effect of several parameters - microstructural and kinetic - is assessed. In addition, the effect of changing structural parameters - such as the MEA structure thickness - is evaluated. This is done to support the work of researchers from the Chemistry Department of Padua. As it will be seen, some results are easily predictable (e.g. smaller electrolyte thickness is preferred), others are less predictable (e.g. increasing the cathode thickness increases the cell performance).

4.1 MEA structure porosity sensitivity analysis

The effect of a change in porosity, both anode and cathode side, is here evaluated. Obviously, the porosity of the electrolyte has not been varied as this is modeled as a dense non-permeable layer. Changes in electrode porosity are difficult to evaluate as it affects both mass diffusion and TPB length. In fact, it is known that volumetric density of PEAS, that is the electrochemical active zone, increases when the electrode porosity decreases; however, the mass diffusion resistance increases in this situation. On the contrary, an increase in the electrode porosity leads to a decrease in mass diffusion resistance, at the expense of the electrochemically active area. In order to optimize SOFCs performance, porosity and particle size need to be carefully balanced [44]. The effect of changes in the electrodes' porosity is shown in Figure 4.1.

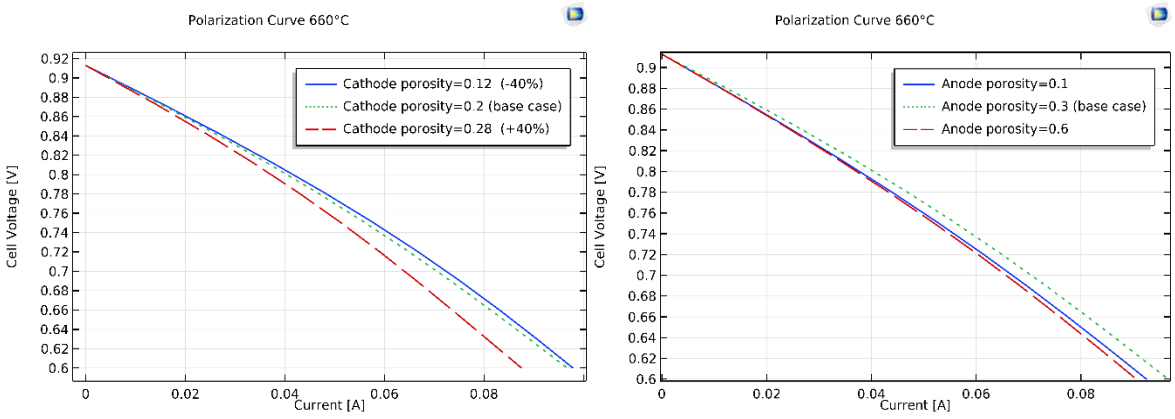

(a) *(b)*

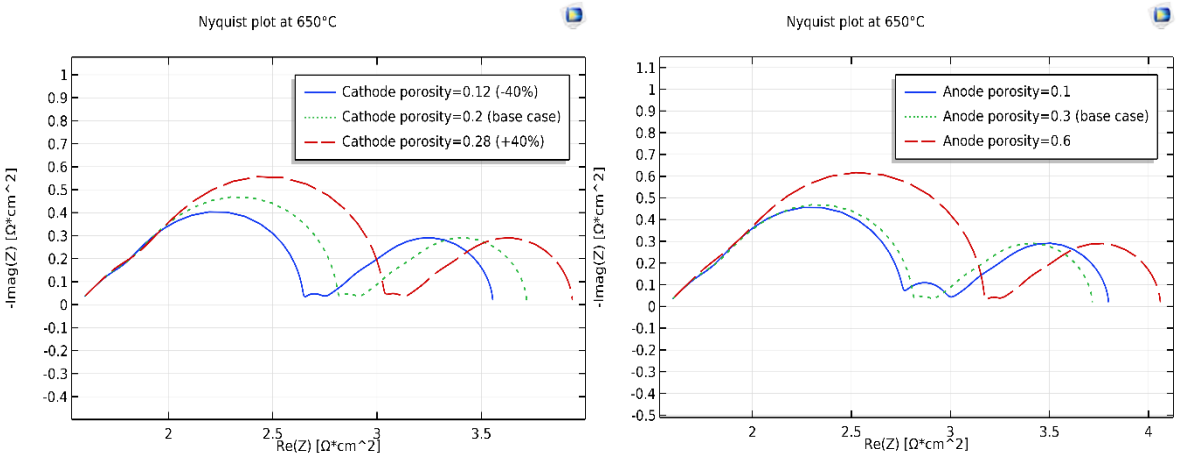

(c) *(d)*

Figure 4.1. *Changes in electrodes porosity. Both PC and EIS are used to characterize the effect.*

Cathode porosity has been varied between ±40% of the base case (0.12/0.2/0.28), while the anode porosity has been varied in a wider range - as explained below - (0.1/0.3/0.6). In order to have a better interpretation, the effect of porosity changes has been visualized both on the Polarization curve and on the Nyquist plot. This holds true for all the other parameters studied in this chapter. As expected, an increase in porosity leads to a decrease in the active area per unit volume. This is reflected, for both electrodes, in the increase of the arc related to the high frequencies in the Nyquist plot. Although the trend is the same for both anode and cathode, this effect is much more pronounced at the cathode. That is mainly for two reasons: firstly, because the cathode is the electrode limiting the cell performance the most (here the molecular oxygen reduction occurs); secondly, because electrodes are strongly different from the microstructural point of view. In fact, the cathode is a composite electrode while the anode is an impregnated electrode. This implies that the particle size of the powders used is very different, and this is reflected both on microstructural electrodes features and TPB length. Moreover, impregnated electrodes (latest generation electrodes) are characterized by longer TPB length compared to classic composite electrodes. Due to these differences, the porosity range analysed is wider in the case of the anode than in the cathode, since small variations in anode porosity lead to undetectable differences in cell performance. The overall cell performance is represented in the polarization curves, Figure 4.1 a) and b). In both cases, an increase in porosity leads to lower performance; this implies that a decrease in mass transport resistance cannot make up for the loss of active area.

Since the analysed polarizations in the PCs are relatively low, the effect of porosity changes at high polarizations has been evaluated as well. In this case, the effect of Concentration Polarizations will be more pronounced. Figure 4.2 shows the effect of high polarizations as a function of porosity.

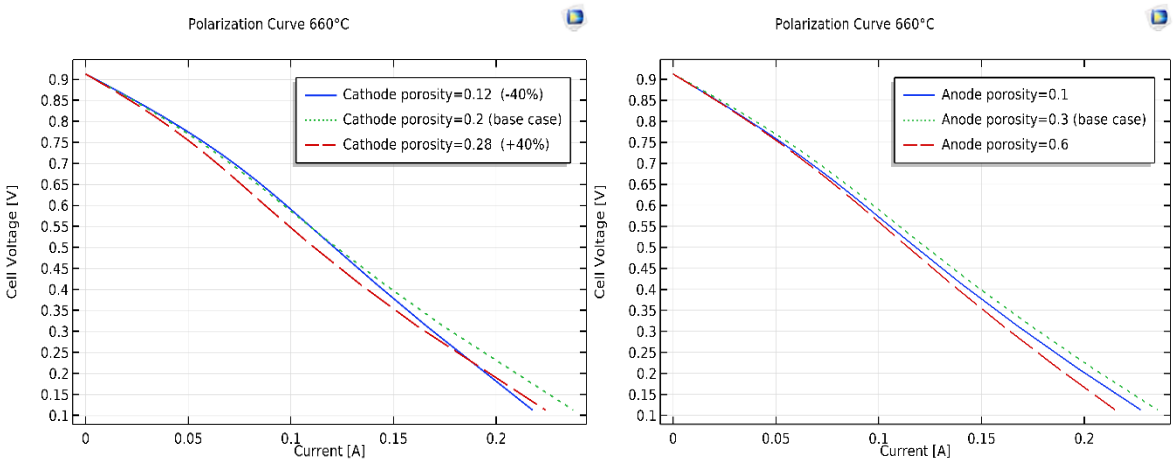

(a) *(b)*

Figure 4.2. *Effect of Concentration Polarizations as function of the porosity cathode side (a) and anode side (b).*

By increasing the polarization of the cell, the effect of changes in porosity is increasingly pronounced. Particularly, at the cathode side, at low polarizations the decrease in porosity leads to an improvement in the performance whereas, at high polarizations, low porosity leads to worse cell performance. In Figure 4.2 a), this is represented by the crossing of the two curves, red and blue. Qualitatively, this phenomenon can be interpreted considering that, by increasing the polarization, there is a greater consumption of oxygen. This implies that, if the concentration gradient increases, the molecular oxygen demand will increase; moreover, the lower the electrode porosity, the greater the resistance to its transport and the lower the cell performance. The opposite holds true as well. Although an increase in polarization makes the effect of a change in porosity more pronounced, at the anode the behaviour remains the same (see Figure 4.2 b)). This is probably due to the fact that the feed is rich in hydrogen. Furthermore, the variation in species concentration also impacts on the local current produced (at the anode) or consumed (at the cathode). This current is calculated by means of the Butler-Volmer concentration dependent equations seen in Paragraph 2.4.3. Therefore, this analysis underlines the difficulty in interpreting complex phenomena, related to each other in strongly non-linear way, which takes place within a SOFC. However, modeling helps to understand these aspects, interpret them and improve design features. The choice of an adequate porosity, typically between 0.2-0.3 for a composite electrode or 0.25-0.4 for an impregnated one, involves the right compromise between transport phenomena and electrochemistry.

Finally, for the sake of completeness, the effect of a change in the anode backbone porosity, assumed to be 0.41 in the base case, is evaluated. The result of this analysis is shown in Figure 4.3.

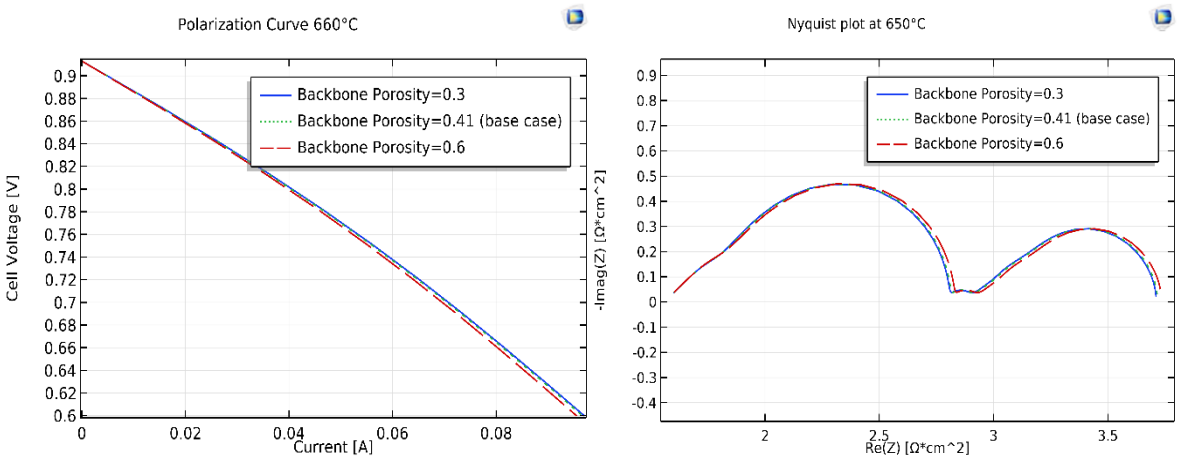

(a) *(b)*

Figure 4.3. *Effect of a change in the anode backbone porosity.*

As expected, the effect of the CGO backbone porosity does not have a big impact on the cell performance. This is because the backbone porosity does not influence the length of the TPB, which is instead determined by the circumference created by sintered coating of Cu nanoparticles on the backbone. Nevertheless, it slightly affects the ionic conductivity of the electrode. Since the anode structure is composed of micrometric CGO particles, the probability of having A type ionic conducting clusters is unitary. Therefore, the resistance offered by the anode to the ionic charge conduction remains marginal compared to the resistance offered by a very thick electrolyte (as in this case).

4.2 MEA structure thickness sensitivity analysis

When investigating the performance of a SOFC, not only the materials used have an impact, but also the geometry used can greatly affect it. In Chapter 2 the most common SOFC designs were shown. Furthermore, it has been specified that the cell used in this thesis is an electrolyte supported button SOFC. Button cells are characterized by low performance, and they are used on laboratory scale to test new materials. Additionally, the cell here used has also the limitation of having a thick electrolyte. Although it provides mechanical resistance to the cell, unfortunately it confers a high ionic charge transport resistance. In fact, to overcome this limitation, the latest generation SOFCs are electrode supported, anode or cathode. The cell performance is here assessed by changing the thickness of the electrodes and electrolyte, respectively. In the last case, the considerations made are quite obvious: the smaller the thickness of the electrolyte, the better the cell performance. When analysing the effect of changing the electrodes thickness, it must be kept in mind that its thinning limits the active zone, while its thickening increases the transport resistance of reacting species.

Therefore, the purpose of this analysis is to determine whether the thicknesses used for this cell - 30 μm electrodes and 1 mm electrolyte - are the optimal ones. The thickness of the cathode is evaluated first; Figure 4.4 shows the effect of cathode thickness on the cell performance.

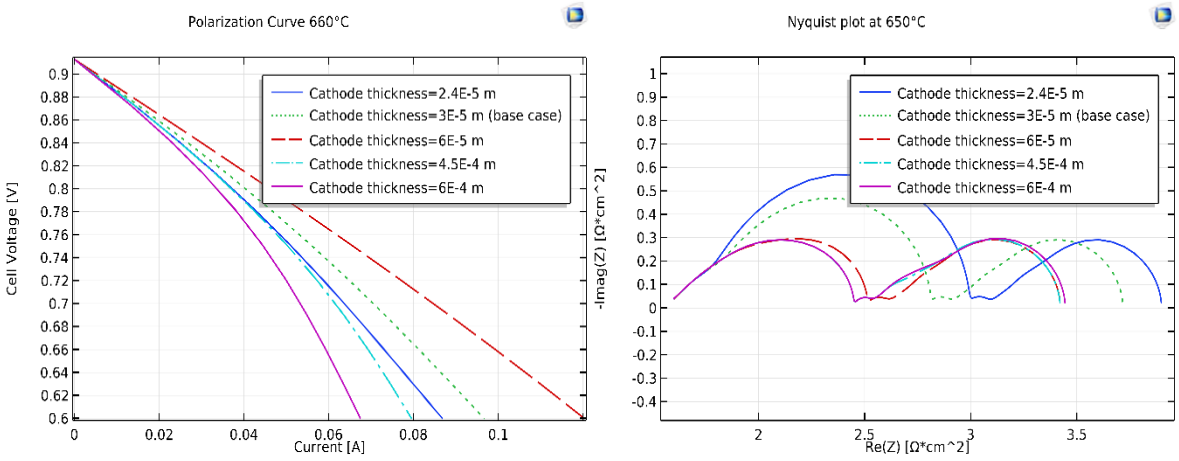

(a) *(b)*

Figure 4.4. *Effect of a change in the cathode thickness.*

The first clearly visible result is that decreasing the cathode thickness leads to a substantial decrease in the cell performance. This is due to the loss of the active area where the oxygen reduction takes place. The second important result is that an increase in the electrode thickness, e.g. doubling it, leads to a sharp increase in the performance. However, it is not possible to increase the thickness freely. In fact, increasing the thickness of about an order of magnitude leads to a sudden drop in performance. Moreover, when the electrode becomes very thick, the right arc in the Nyquist plot (characterized by low frequencies) tends to deform. This means that, beyond the active layer, an increase in thickness only leads to greater species diffusion resistance. In order to obtain the optimal cathode thickness, by means of the model, it was necessarily to estimate the maximum electrochemically active thickness of the electrode. After some parametric sweeps, the optimal thickness was determined to be between $80 - 85\ \mu m$ (about three times the base case). This range was then analysed by carrying out a 1 μm thickness parametric sweep. The result of this analysis is shown in Figure 4.5. Since the curves are very close to each other, in order to see the maximum thickness beyond which the performance no longer grows, Figure 4.5 has been magnified. The maximum performance is obtained at 82 μm. As the model suggests, the cathode requires a thickness about three times greater than the base case, in order to increase the performance of the cell. Once again, this result can be obtained through modeling without the need of several experimental tests that require time and money.

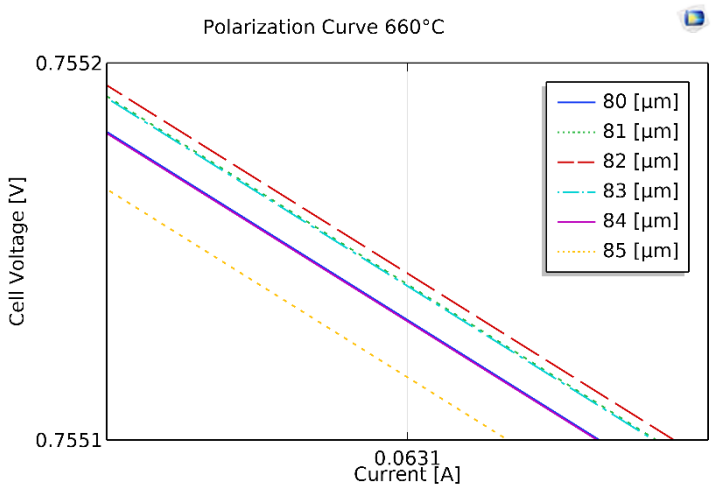

Figure 4.5. *Magnification of the cathode thickness effect in the range* $80 \div 85\ \mu m$.

The same analysis was conducted for the anode; in this case, the optimal thickness suggested by the model was evaluated as well. Figure 4.6 shows the effect of the anode thickness variation on the cell performance.

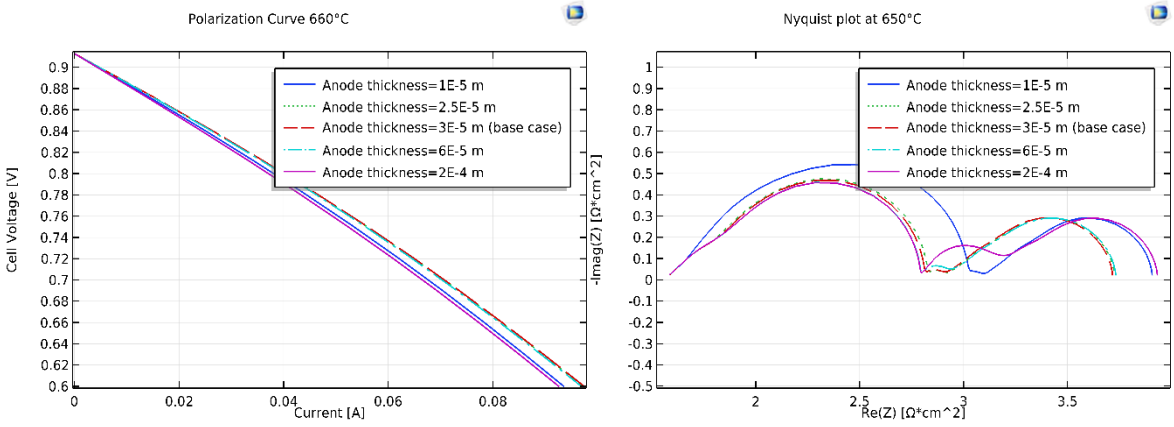

(a) *(b)*

Figure 4.6. *Effect of a change in the anode thickness.*

Although the trend is the same as that seen for the cathode, the effect is much less pronounced. In fact, as already mentioned, the cathode is the electrode that limits the performance of the cell, where the molecular oxygen reduction (kinetically limited) occurs. In addition, the two electrodes have very different morphologies as previously discussed. The same considerations made for the cathode can be applied to the anode. Through a parametric analysis, it has been found that the optimal anode thickness is between $30 - 35\ \mu m$. Figure 4.7 shows that the optimal thickness found is $34\ \mu m$.

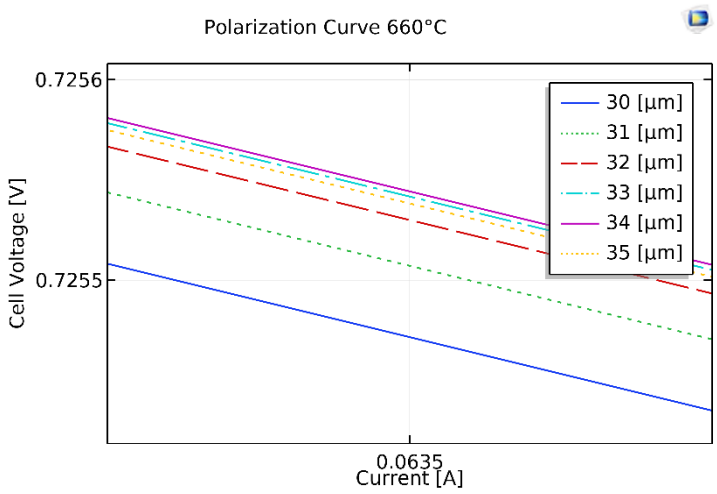

Figure 4.7. *Magnification of the anode thickness effect in the range* $30 \div 35\ \mu m$.

This result, net of the assumptions made in the model, suggests that the anode design is optimal for this cell. On the other hand, the cathode is strongly undersized.
Finally, the effect of the electrolyte thickness change was assessed as well. The result of this analysis corresponds to what expected: the electrolyte must be as thin as possible, ensuring excellent ionic conductivity and gas tightness. Therefore, during SOFC design, it is necessary to find the right trade-off between these two features. In Figure 4.8, the effect of changes in the electrolyte thickness is shown.

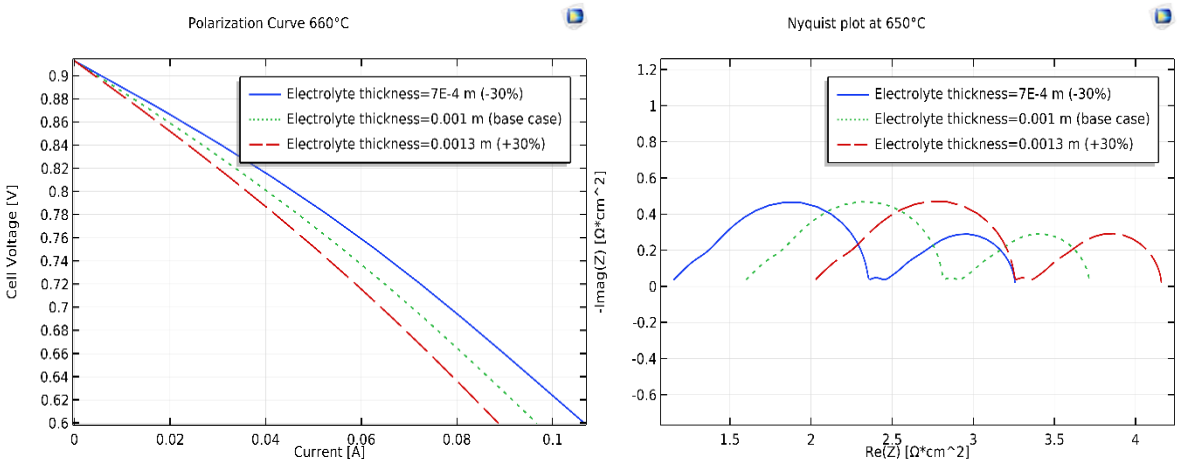

(a) *(b)*

Figure 4.8. *Effect of a change in the electrolyte thickness.*

When the electrolyte thickness is reduced down to $5 - 10\ \mu m$, a new design for the electrode/electrolyte structure is needed. As the thin electrolyte can no longer be the mechanically supporting component, one of the porous electrodes must take over this

function. SOFCs based on thin electrolytes have already been tested and exhibited excellent electrochemical performance [45]. In the Nyquist plot, the thickness variation translates into a shift in the curves. This is caused by an increase/decrease in the cell's Ohmic resistance, which corresponds to a shift in the curves, to the left or to the right respectively. As for the cell performance, a decrease in the ionic charge transport resistance leads to a considerable increase in the performance while, decreasing the electrolyte thickness, the opposite effect occurs (see Figure 4.8 a)). Nowadays, SOFCs are produced with micrometric electrolyte thickness to avoid the aforementioned problem.

4.3 Gold paste features sensitivity analysis

In this section the microstructural parameters related to the gold paste have been subjected to a sensitivity analysis. Unfortunately, the gold paste features are unknown. However, a distinctive characteristic of the gold paste layer is that it does not have to strongly impact the cell's performance. Therefore, it is expected that changes in the analysed parameters will not lead to large changes in performance. Furthermore, the variation of these parameters will only influence the supply of the reacting species to the electrodes, i.e. transport phenomena, since no electrochemical reaction occurs inside the gold paste. In Figure 4.9 the effect of changes in the gold paste thickness, porosity and permeability is assessed. Notice that, the gold paste permeability was estimated during the PC optimization, as described in Paragraph 3.2.

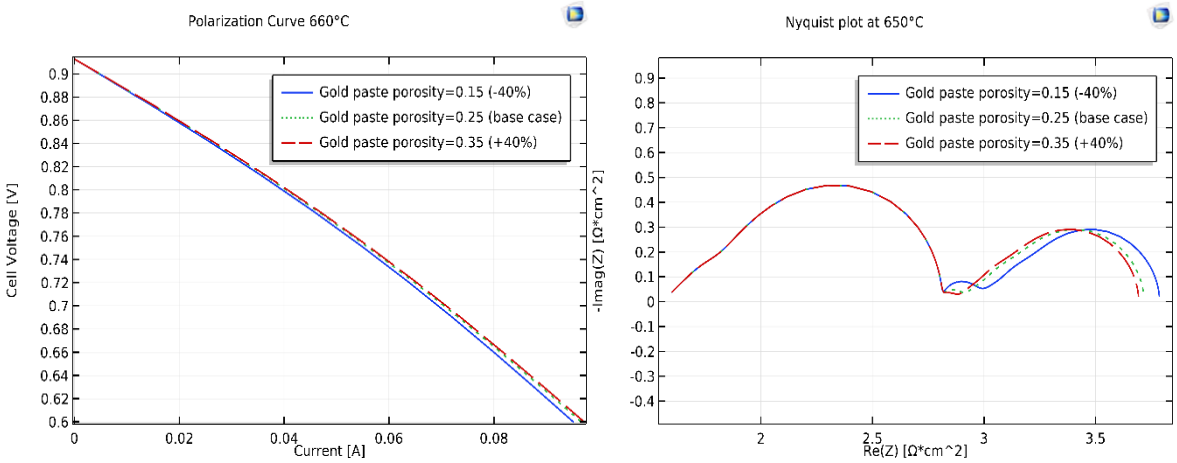

(a) *(b)*

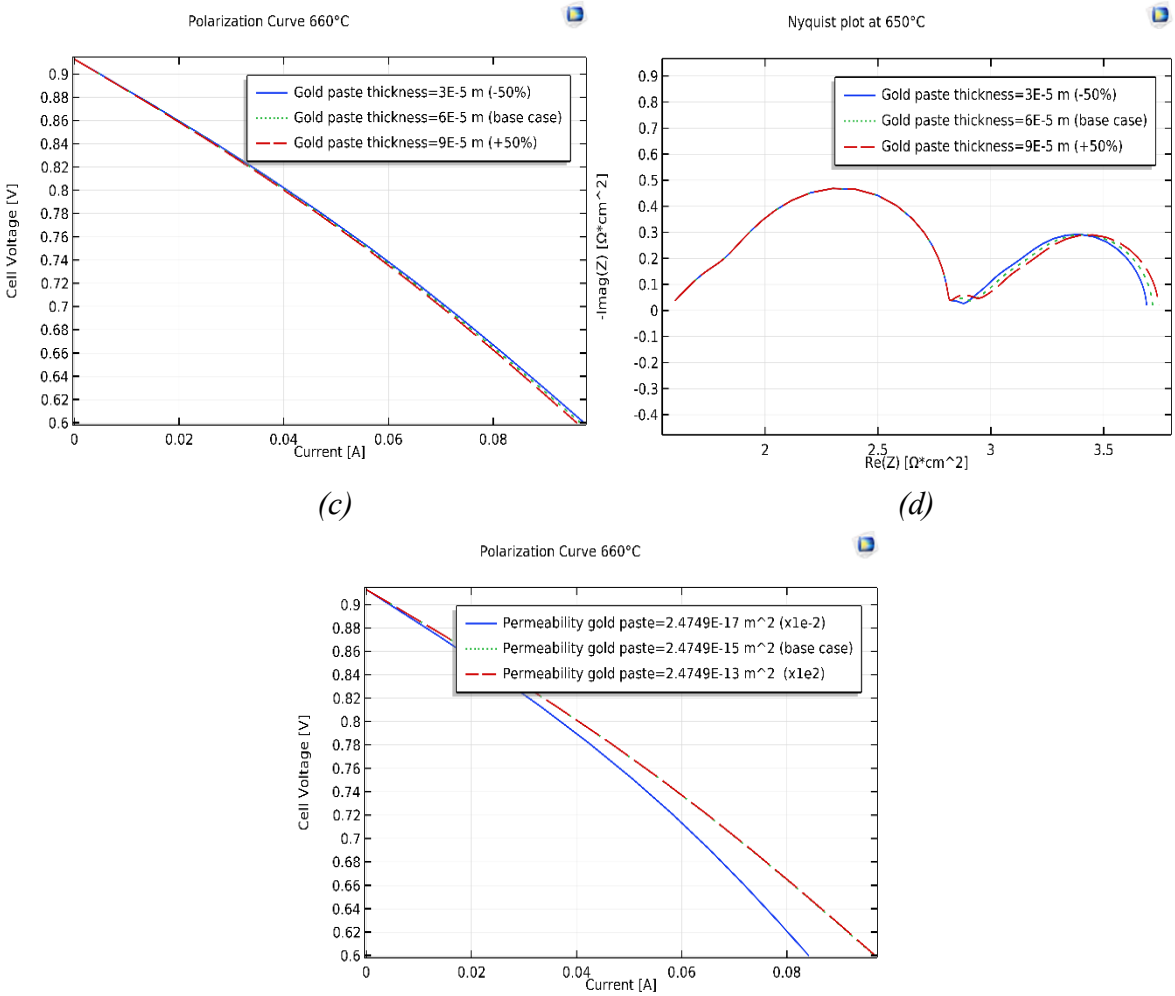

Figure 4.9. *Effect on cell's performance by changing the porosity (a,b), thickness (c,d) and permeability (e) of the gold paste.*

As expected, the gold paste does not significantly affect the cell's performance and its only effect is to increase or decrease the resistance to species transport phenomena. In fact, the variations of these parameters lead to small changes in the low frequency arc of the Nyquist plot. Notice that, as for the permeability, its effect cannot be shown in the Nyquist plot since the "Free and Porous Media Flow" module is not solved during AC impedance study. Despite this, the permeability will surely affect the low frequency arc. From Figure 4.9 e) it is possible to notice that an increase in permeability - with respect to the optimized base case - does not entail any variation in performance. This means that the gold paste does not influence the supply of reacting species towards the electrodes. On the contrary, if the permeability is decreased by two order of magnitude, its effect becomes crucial acting as a bottleneck for species transport phenomena.

In order to qualitatively represent the effect of permeability in the Nyquist plot, the values of the effective binary diffusion coefficients in the gold paste domains have been increased or decreased by an order of magnitude, as shown in Figure 4.10.

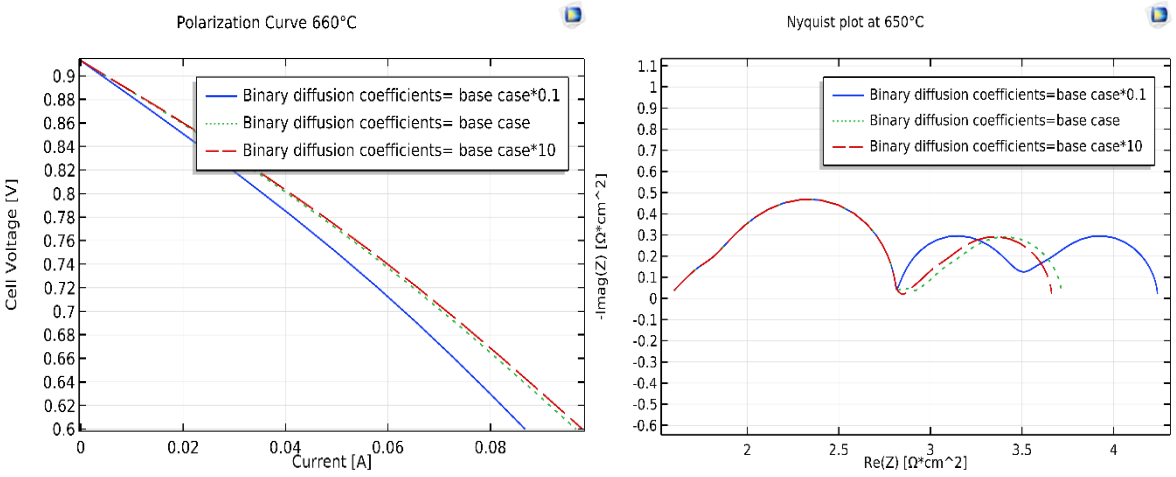

(a) *(b)*

Figure 4.10. *Effect of changes in the effective diffusion binary coefficients in the gold paste domain.*

The effect seen in Figure 4.9 e) and Figure 4.10 a) is very similar. Particularly, the decrease in the effective binary diffusion coefficients leads to a distortion of the EIS curve. In fact, a third arc, usually flat and not visible, appears. Qualitatively, this can be interpreted as a significant increase in the transport phenomena resistance, and it would explain the bottleneck behaviour of the gold paste. However, both the model and the experimental data suggest that the gold paste layer does not significantly influence the cell's performance.

4.4 Kinetic parameters sensitivity analysis

Exchange current densities, $i^0_{A/C}$, in electrochemical reactions are the analogous of the rate constant in chemical reactions. Unlike the rate constants, exchange current density is concentration dependent (see equation 3.3), which means that its effect is harder to interpret. Generally speaking, when designing a new SOFC, it is important to increase the values of the exchange current densities to improve kinetics performance. A direct way to maximize $i^0_{A/C}$ is to increase the available active sites per unit area and minimize the activation barrier of the electrochemical reactions involved. The latter strongly depends on the choice of the electrocatalyst used. Moreover, they are strongly influenced by temperature and composition. Given the difficulty in correlating the exchange current densities to the chemical, physical and geometric features of the cell - which would require a specific study

and model - in this paragraph only the effect of their variation on cell's performance is assessed. Figure 4.11 shows how changes in the exchange current densities affect the cell.

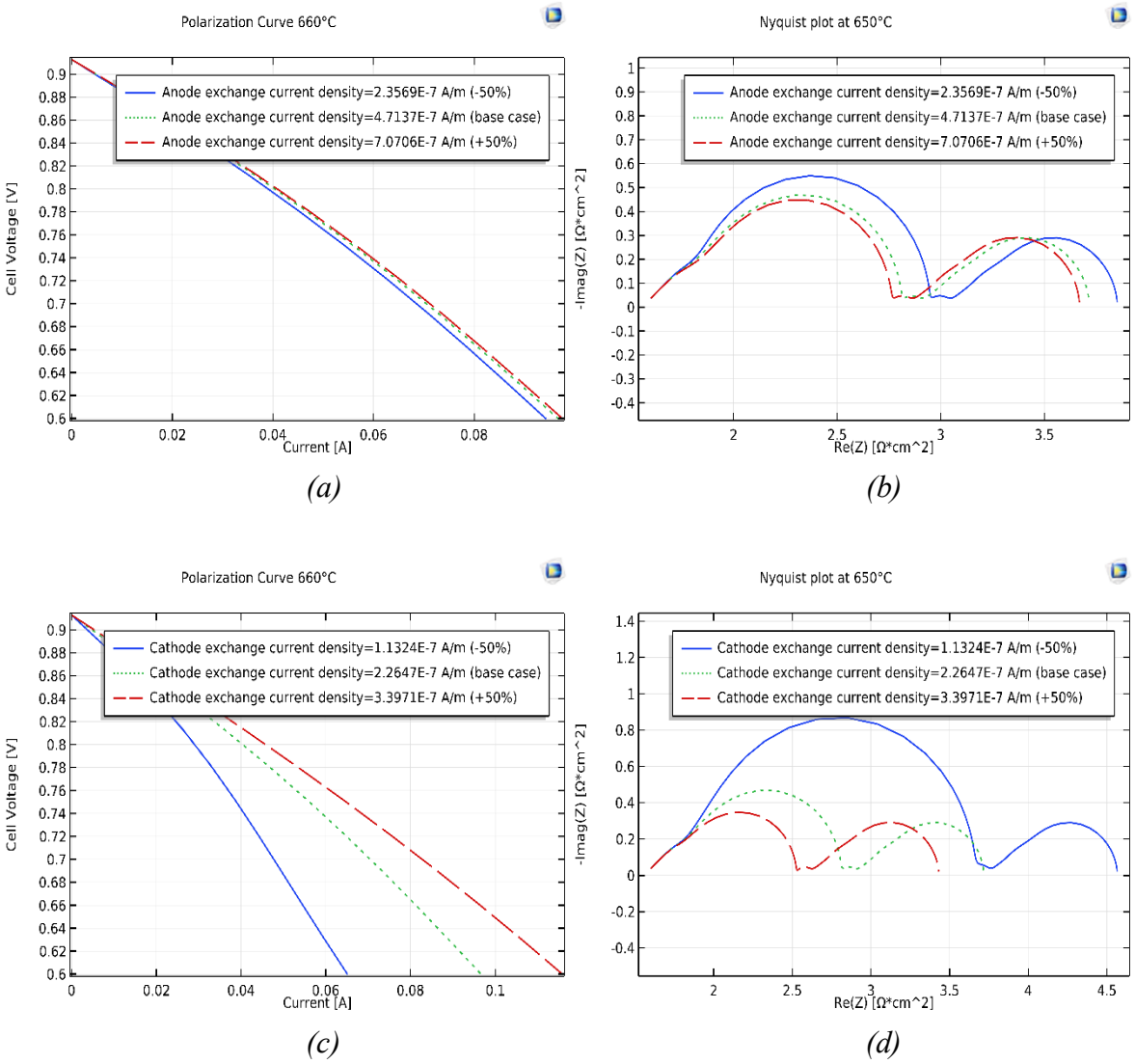

Figure 4.11. *Effect of the exchange current densities on cell's performance. The values of the current densities in EIS and PC are slightly different because of the difference in temperature (see 3.2)*

The results are not surprising. In fact, as expected, increasing the exchange current densities always has a positive effect on cell's performance. On the contrary, their decrease has the opposite effect for the aforementioned reasons. Graphically, this translates into a variation (compression or enlargement) of the high frequency arc in the Nyquist plot, or in a greater or smaller current delivered at the same voltage in PCs. Although the trend in Figure 4.11 a) and b) and Figure 4.11 c) and d) is the same, the effect is much more pronounced on the cathode side. Also, this result is quite expected. In fact, as already mentioned, the cathode limits the cell performance as the molecular oxygen reduction is kinetically inhibited. From

a chemical point of view, this translates into a high activation barrier to overcome in order for the reaction to occur. For these reasons, nowadays the search of new materials capable of promoting oxygen reduction is very active.

4.5 Contact angles sensitivity analysis

The last parametric analysis performed was done to evaluate the effect of contact angles between particles. Since there is no link in the theories used between porosity and contact angles, these parameters are not expected to influence transport phenomena. On the other hand, they will influence the TPB length and the conductivities. The variation of the contact angles between Cu/CGO particles and LSCF/CGO particles can be seen in Figure 4.12.

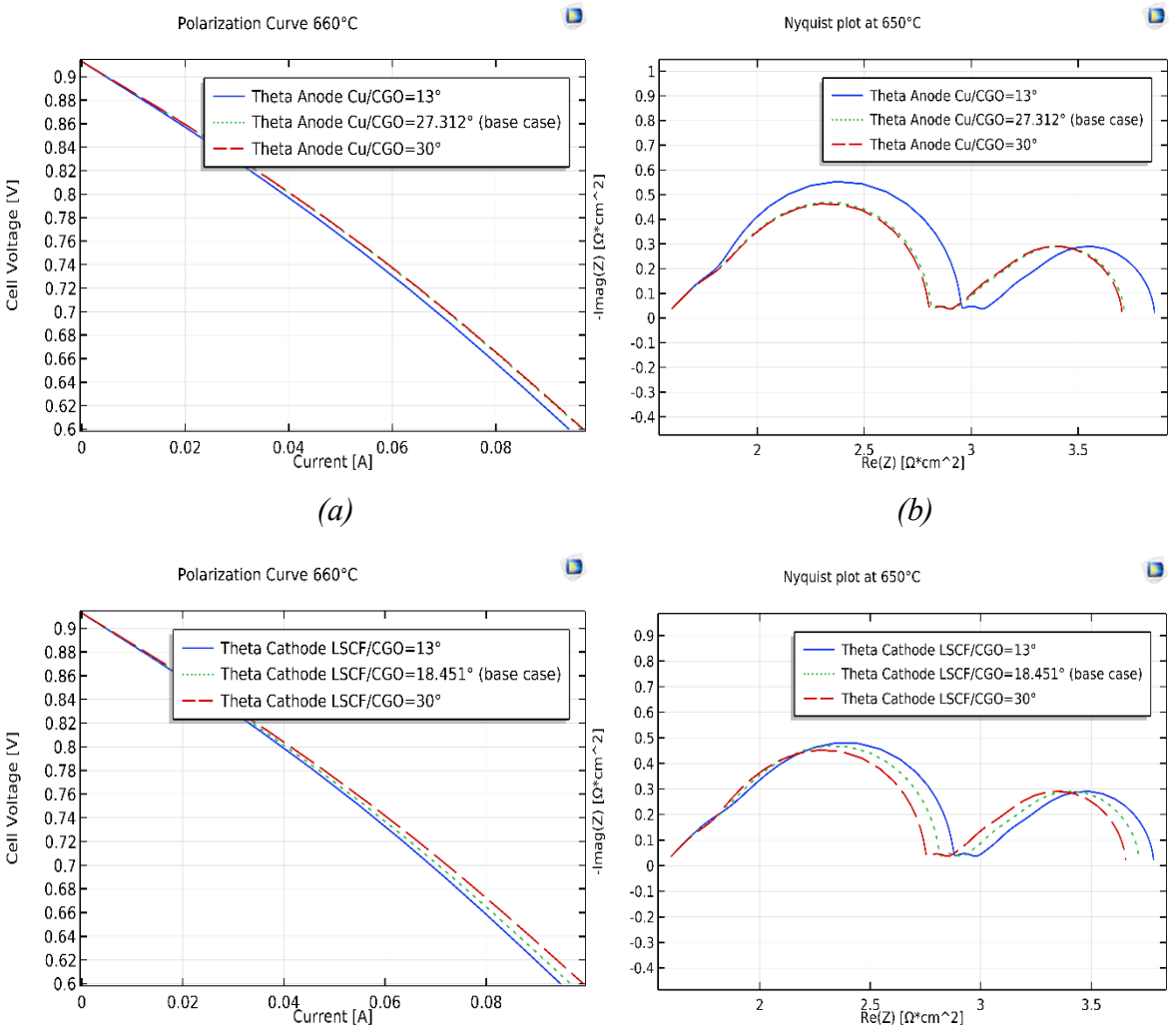

Figure 4.12. *Effect of the contact angles on cell's performance*

Although the trend is the same, also in this case the effect is more pronounced in the cathode side. Specifically, when the contact angle decreases, both the TPB length and conductivities decrease. That happens because, by decreasing the contact surface between particles, the TPB will decrease and, at the same time, the conductivity (especially the ionic one) will decrease due to a bottleneck effect in the charge conductivity. The latter can be explained because low contact angle behaves like a restriction, strongly limiting inter-particle conductivity (see Paragraph 2.4.4). Therefore, for both the contact angles, a decrease in performance is seen (Figure 4.12 a) and c)) with an extension of the high frequency arc (Figure 4.12 b) and d)). The opposite effect occurs by increasing the contact angle. In real applications, electrodes characterized by extremely low contact angles will tend to be very permeable but will show a limited active area and low ionic conductivity. On the other hand, electrodes characterized by large contact angles, will have longer TPB length and higher ionic conductivity but they will behave as a dense non-permeable block. For those reasons, the final characteristics of the electrode are not only determined by the materials used but also by the manufacturing technique.

Conclusions

This work is the result of a collaboration between the Industrial Engineering Department and the Chemical Science Department of the University of Padua. In this thesis, a model able to describe an electrolyte supported button SOFC, produced and characterized by the researchers of the Chemistry department, has been developed. The model was first built and then analysed via COMSOL Multiphysics, comparing the calculated results to the experimental data. Most of the unknown parameters were obtained through an optimization process, which allows to derive the optimal parameters needed to fit the experimental curves. The similarity between calculated and experimental results has ensured the effectiveness of the model. Two characterization methods were used in order to validate the model: Electrochemical Impedance Spectroscopy (EIS) and Polarization Curve (PC). Once the model has been validated, a parametric study was carried out to study the influence of some key parameters on SOFC performance. This analysis has particularly focused on the effect of the variation of microstructural and geometrical parameters, such as the porosity of the electrodes and the thicknesses of the MEA structure. Moreover, different properties of the gold paste interconnect and kinetic parameters have been analysed.
Among the results obtained, some were easily predictable while others, suggested by the model, could help in developing high performance SOFCs with new designs. Some of the most distinctive results obtained are here reported:

- The porosity of the electrodes is crucial in the performace of the cell. In fact, porosity affects both transport phenomena and the spatial distribution of the electrochemically active area, within the porous domain. Values above or below the optimal porosity range, usually between 0.2-0.4 depending on the electrode's morphology, can compromise the performance of the cell.

- The thickness of the electrodes - specifically the cathode - is a key parameter in the design of new SOFCs. The search of an optimal electrode thickness allows the cell to maximize its active area without offering further and unnecessary resistance to the transport of species. From this work it emerges that the cell design analysed should be improved. Specifically, while the thickness of the anode turned out to be well designed, the thickness of the cathode proved to be strongly undersized.

- The search of new active materials at lower temperatures is crucial to make SOFCs more attractive in different applications. This translates into finding new electrocatalysts, less expensive and active at low temperature (less than 500-600°C). This is particularly true for the cathode, the most limiting domain of a SOFC, where the molecular oxygen reduction (characterized by high activation energy) takes place.

- The manufacturing methods of the electrodes have a strong impact on the final performance of the cell. In fact, their influence on the final microstructural characteristics of the electrodes affect both the TPB and the mass transport phenomena.

Future applications concern the use of this model:

- To obtain much more information about kinetic parameters - such as the dependencies on composition and temperature for the exchange current densities - when new materials are used

- To estimate the behaviour of new cell designs, composed of new materials or fed with different reactants, such as CH_4 or CO.

Furthermore, a collaboration between the two departments can lead to the characterization of the electrodes' porosity, leaving kinetic and geometrical parameters as the only degrees of freedom to evaluate.

Appendix

- *Table of b_k parameters*

	b_0	b_1	b_2	b_3	b_4	b_5	b_6
Ar	-3.0982	978.51	-922.67	912.64	-593.76	217.79	-33.919
H_2O	-6.7541	244.93	319.5	-522.38	348.12	-126.96	19.591
H_2	15.553	299.78	-244.34	249.41	-167.51	62.966	-9.9892
N_2	1.2719	771.45	-809.2	832.47	-553.93	206.15	-32.43
O_2	-1.6918	889.75	-892.79	905.98	-598.36	221.64	-34.754

- *Table of Fuller diffusion volumes $v_i[m^3]$*

Ar	H_2	O_2	N_2	H_2O
16	6.12	16.3	18.5	13.1

- *Parameters used to evaluate the Anode net electronic conductivity*

Parameter	*Value*	*Reference*
λ_{crit}	0.5	[37]
$f_2 = R_{film}/R_{eff}$	0.575	[37]*
τ_s	2.8	[37]#

*Mean value assuming the contact angle between Cu particles equal to 15°

#Mean value considering the porosity of the electrode varies between 0.2 and 0.4.

Nomenclature

Glossary

$C_{R/O}$	Normalized concentration of reduced/oxidized species
$D_{ij,K}$	Knudsen binary diffusion coefficient $[m^2/s]$
D_{ij}	Fuller binary diffusion coefficient $[m^2/s]$
D_{ij}^{eff}	Effective binary diffusion coefficient $[m^2/s]$
D_p	Mean particle diameter $[m]$
E^0	Potential at standard conditions $[V]$
E_a	Activation energy
F_b	Volume force vector $[N/m^3]$
I_0	Current amplitude $[A]$
J_i	Mass flux for the generic species *i* $[kg/(m^2 \cdot s)]$
$P^{e,io}$	Probability of forming *e/io* conducting path
Q_{br}	Brinkman source term $[kg/(m^2 \cdot s)]$
V_0	Voltage amplitude $[V]$
Z_0	Impedance amplitude $[\Omega\, m^2]$
$Z_{k,l}$	Coordination number
a_i	Activity coefficient of species *i*
d_p	Mean pore diameter $[m]$
i^0	Exchange current density $[A/m]$
n_i^V	Number of *i* particles per unit volume
p_i	Partial pressure of species *i* $[Pa]$
$r_{p,j}$	Mean pore radius (*j=A,C*) $[m]$
w_i	Mass fraction for the generic species *i*
β_F	Effective dynamic viscosity in porous domains $[Pa \cdot s]$
ε_j	Porosity (*j=A,C,Au*)
λ_{DPB}^{eff}	Effective DPB per unit length $[1/m^2]$
λ_{TPB}^{eff}	Effective TPB per unit length $[1/m^2]$
ν_i	Stoichiometric coefficient of species *i*
$\sigma_{i,j}$	Conductivity (*i= e,io ; j=material or domain*) $[S/m]$
σ_i^0	Bulk conductivity of material $[S/m]$
ψ_i	Volumetric solid fraction of *i* particles (*i=Cu.CGO,LSCF*)
ϕ_{el}	Electrolyte potential

ϕ_s	Electrostatic potential $[V]$
I	Identity matrix
K	Permeability $[m^2]$
$\Delta\tilde{G}^0$	Molar Gibbs free energy at standard condition $[J\ mol^{-1}]$
$\Delta\tilde{G}_R$	Molar Gibbs free energy $[J\ mol^{-1}]$
A	Pre-exponential factor
E	Reversible voltage potential $[V]$
F	Faraday constant $[C\ mol^{-1}]$
I	Current $[A]$
MW_i	Molecular weight for the generic species *i* $[kg/mol]$
R	Ideal gas constant $[J\ mol^{-1}\ K^{-1}]$
S	Source/Sink term for species and charge
T	Temperature $[K]$
V	Voltage $[V]$
Z	Impedance $[\Omega\ m^2]$
i	Current density $[A\ m^{-2}]$
i	Current density $[A/m]$
u	Velocity vector $[m/s]$
z	Number of electrons
α	Electron transfer coefficient
δ	Thickness of the interface between sintered particles $[m]$
η	Overpotential $[V]$
μ	Bruggeman factor
ρ	Fluid density $[kg/m^3]$
τ	Tortuosity
ω	Frequency [Hz]
ϕ	Phase shift $[rad]$

Subscripts

A/C	Anode and cathode side
A	Anode
C	Cathode
N	Nernst
R	Reaction
TOT	Total value of a generic parameter
$cell$	Relative to the cell

e	Electronic conducting phase
eq	Value at equilibrium condition
io	Ionic conducting phase
m	Molten state

Superscripts

$\sim$	Molar unit
eff	Effective property
ter	Inter-particle
tra	Intra-particle

Abbreviations

lb	Lower bound
ub	Upper bound
AC	Alternating current
AFC	Alkaline Fuel Cell
$CERMET$	Material composed by metallic and ceramic solid phase
CGO	Gadolinium doped Ceria
DC	Direct current
$DMFC$	Direct Methanol Fuel Cell
DPB	Double Phase Boundary
ECM	Equivalent Circuit Model
EIS	Electrochemical Impedance Spectroscopy
FEM	Finite Element Method
FPM	First Principle Model
$LSCF$	Lanthanum Strontium Cobalt Ferrite
LSM	Strontium stabilized Lanthanum Manganite
$MCFC$	Molten Carbonate Fuel Cell
MEA	Membrane Electrode Assembly
$MIEC$	Mixed ionic-electronic conductors
MSR	Methane steam reforming reaction
OCV	Open circuit Voltage
$PAFC$	Phosphoric Acid Fuel Cell
PC	Polarization Curve
$PEAS$	Potentially Electrochemically Active Sites

$PEMFC$	Proton Exchange Membrane Fuel Cell
$SOFC$	Solid Oxide Fuel Cell
TPB	Three Phase Boundary
WGS	Water Gas Shift reaction
YSZ	Yittria stabilized Zirconia

Bibliography and Sitography

1. https://ec.europa.eu/eurostat/statistics-explained/index.php/Renewable_energy_statistics
2. Solid Oxide Fuel Cells modelling under steady-state and forced oscillation regimes- Tesi di laurea,Nicola Zanetti, University of Padua 2016/2017.
3. Optimal Design and Operation of Solid Oxide Fuel Cell Systems for Small -scale Stationary Applications- Thesis by Robert J. Braun, University of Wisconsin –Madison, 2002.
4. www.hydrogeneurope.eu/fuel-cells.
5. Semicelle SOFC: Studio e Produzione di elettroliti con processi a basso impatto ambientale-phd thesis-Patrizia Mangifesta, University of Bologna, 2009.
6. Fuel Cell Fundamentals, 3rd edition, Wiley - O'Hayre, Ryan, Suk-Won Cha, Whitney Colella and Fritz B. Prinz.
7. Finite Element Method (FEM) Model and Performance Analysis of Solid Oxide Fuel Cells – Helge Ingolf, Geisler, KIT Scientific Publishing, 2019.
8. Chemical Reacting Flow: Theory, Modeling, and Simulation 2nd edition, Wiley 2017– Robert J. Kee, Michael E. Coltrin, Peter Glarborg.
9. Solid Oxide Fuel Cell microstructure and performance modelling, phd thesis by Khalil Rhazaoui, Imperial college of London 2013.
10. Progettazione e sviluppo di una cella a combustibile ad ossidi solidi alimentata a biogas: dai materiali al dispositivo - Giovanni Carollo, University of Padua 2016/2017.
11. Milewski, Jarosław & Lewandowski, J. (2010). Analysis of Design and Construction of Solid Oxide Fuel Cell in Terms of their Dynamic Operation. Archivum Combustionis Vol. 30.
12. Introduction to corrosion science, Springer Science & Business Media, 2010 – E. McCafferty
13. www.comsol.com/blogs/electrochemical-impedance-spectroscopy-experiment-model-and-app/
14. Rodríguez, J.; Palmas, S.; Sánchez-Molina, M.; Amores, E.; Mais, L.; Campana, R. Simple and Precise Approach for Determination of Ohmic Contribution of Diaphragms in Alkaline Water Electrolysis. *Membranes* **2019**, *9*, 129.
15. Development and implementation of techniques to characterize Solid Oxide Fuel Cells-Thesis by Gisela Auxiliadora Cepeda Arque- University of Padua 2016/2017.
16. www.simscale.com/docs/content/simwiki/fea/whatisfea.html
17. www.comsol.com/blogs/how-to-set-up-a-mesh-in-comsol-multiphysics-for-cfd-analyses/

18. Tseronis, K., Fragkopoulos, I. S., Bonis, I., & Theodoropoulos, C. (2016). Detailed Multi-dimensional Modeling of Direct Internal Reforming Solid Oxide Fuel Cells. Fuel Cells, 16(3), 294–312.
19. Guk, E., Kim, J.-S., Ranaweera, M., Venkatesan, V., & Jackson, L. (2018). In-situ monitoring of temperature distribution in operating solid oxide fuel cell cathode using proprietary sensory techniques versus commercial thermocouples. Applied Energy, 230, 551–562.
20. Hodjati-Pugh, O., Dhir, A., & Steinberger-Wilckens, R. (2017). Three-Dimensional Modelling of a Microtubular SOFC: A Multiphysics Approach. ECS Transactions, 78(1), 2659–2672.
21. Todd, B., & Young, J. B. (2002). Thermodynamic and transport properties of gases for use in solid oxide fuel cell modelling. Journal of Power Sources, 110(1), 186–200.
22. Bertei, A. Mathematical Modeling of Solid Oxide Fuel Cells. Ph.D. Thesis, University of Pisa.
23. Nerat, M., & Juričić, Đ. (2016). A comprehensive 3-D modeling of a single planar solid oxide fuel cell. International Journal of Hydrogen Energy, 41(5), 3613–3627.
24. Andersson, M., Yuan, J., & Sundn, B. (2012). SOFC modeling considering electrochemical reactions at the active three phase boundaries. International Journal of Heat and Mass Transfer, 55(4), 773–788.
25. Ighodaro, Scott, K. and Xing, L. (2017) An Isothermal Study of the Electrochemical Performance of Intermediate Temperature Solid Oxide Fuel Cells. Journal of Power and Energy Engineering, 5, 97-122.
26. Magar, Y. N., & Manglik, R. M. (2007). Modeling of Convective Heat and Mass Transfer Characteristics of Anode-Supported Planar Solid Oxide Fuel Cells. Journal of Fuel Cell Science and Technology, 4(2), 185.
27. www.sigmaaldrich.com/catalog/product/aldrich/704253?lang=it&region=IT
28. Xia, C., Wang, B., Ma, Y., Cai, Y., Afzal, M., Liu, Y., … Zhu, B. (2016). Industrial-grade rare-earth and perovskite oxide for high-performance electrolyte layer-free fuel cell. Journal of Power Sources, 307, 270–279.
29. Mechanical Properties of La0.6Sr0.4Co0.2Fe0.8O3 Fuel Cell Electrodes-Thesis by Zhangwei Chen, Imperial College London 2014.
30. www.fuelcellmaterials.com/products/powders/electrolyte-powders/electrolyte-gadolinium-doped/gadolinium-doped-ceria-10-gd-tape-cast-grade-powder/
31. Chen, D., Lin, Z., Zhu, H., & Kee, R. J. (2009). Percolation theory to predict effective properties of solid oxide fuel-cell composite electrodes. Journal of Power Sources, 191(2), 240–252.
32. Chen, D., Hu, B., Ding, K., Yan, C., & Lu, L. (2018). The Geometry Effect of Cathode/Anode Areas Ratio on Electrochemical Performance of Button Fuel Cell Using Mixed Conducting Materials. Energies, 11(7), 1875.

33. Chen, D., Wang, H., Zhang, S., Tade, M. O., Shao, Z., & Chen, H. (2015). Multiscale model for solid oxide fuel cell with electrode containing mixed conducting material. AIChE Journal, 61(11), 3786–3803.
34. Chen, D., He, H., Zhang, D., Wang, H., & Ni, M. (2013). Percolation Theory in Solid Oxide Fuel Cell Composite Electrodes with a Mixed Electronic and Ionic Conductor. Energies, 6(3), 1632–1656.
35. Vijay, P., Tadé, M. O., Shao, Z., & Ni, M. (2017). Modelling the triple phase boundary length in infiltrated SOFC electrodes. International Journal of Hydrogen Energy, 42(48), 28836–28851.
36. Ding, D., Zhu, W., Gao, J., & Xia, C. (2008). High performance electrolyte-coated anodes for low-temperature solid oxide fuel cells: Model and Experiments. Journal of Power Sources, 179(1), 177–185.
37. Hardjo, E. F., Monder, D. S., & Karan, K. (2013). An Effective Property Model for Infiltrated Electrodes in Solid Oxide Fuel Cells. Journal of the Electrochemical Society, 161(1), F83–F93.
38. Skinner, S. J., & Kilner, J. A. (2003). Oxygen ion conductors. Materials Today, 6(3), 30–37.
39. Shi, Y., Cai, N., Li, C., Bao, C., Croiset, E., Qian, J., … Wang, S. (2008). Simulation of Electrochemical Impedance Spectra of Solid Oxide Fuel Cells Using Transient Physical Models. Journal of The Electrochemical Society, 155(3), B270.
40. Raikova, Gergana & Carpanese, M.Paola & Stoynov, Z. & Viadikova, D. & Viviani, M. & Barbucci, Antonio. (2009). Inductance correction in impedance studies of solid oxide fuel cells. Bulgarian Chemical Communications. 41. 199-206.
41. Comsol Optimization Module User's Guide
42. Adler, S. B. (1996). Electrode Kinetics of Porous Mixed-Conducting Oxygen Electrodes. Journal of The Electrochemical Society, 143(11), 3554.
43. Fabbri, E., Bi, L., Pergolesi, D., & Traversa, E. (2011). High-performance composite cathodes with tailored mixed conductivity for intermediate temperature solid oxide fuel cells using proton conducting electrolytes. Energy & Environmental Science, 4(12).
44. Shi, J., & Xue, X. (2010). CFD analysis of a symmetrical planar SOFC with heterogeneous electrode properties. Electrochimica Acta, 55(18), 5263–5273.
45. Will, J. (2000). Fabrication of thin electrolytes for second-generation solid oxide fuel cells. Solid State Ionics, 131(1-2), 79–96.
46. Steele, B. C. H., & Heinzel, A. (2001). Materials for fuel-cell technologies. Nature, 414(6861), 345–352.
47. https://www.comsol.com/blogs/current-distribution-interface-use/